UNIVERSITÄT DUISBURG ESSEN

Offen im Denken

University of Duisburg-Essen

Faculty of Chemistry

Physical Chemistry

WS 2025/2026

Setup and Evaluation on the EC-STM Mode of an Agilent SPM 5500 for the Investigation of a Gold Sample with Unknown Surface Structure

Thesis to obtain the academic degree Master of Science

Submitted by:

Nikolas Milchers

M. Sc. Chemie

Matriculation number: 3088082

Supervisors:

First: Prof. Dr. Katrin F. Domke

Second: Prof. Dr. Jochen Gutmann

Date of issue: 26. June 2025 Submission deadline: 25. December 2025

Colophon
This document was typeset with the help of KOMA-Script and LaTeX using the kaobook class.
The source code of this book is available at:
`https://github.com/fmarotta/kaobook`
For this work, I rewrote parts of the code, to meet the standards of the university Duisburg-Essen.

AI-based Tools
As part of this thesis, DeepL and ChatGPT 5 were used for grammar, spell checking and to support translation. ChatGPT was used for research some papers and finding sources in combination with Google Scholar.

Reference System
This document uses a dual reference system to distinguish between literary sources and supplementary notes. Citations of literary or academic sources are presented in a numerical format like »[1]«, corresponding to entries in the bibliography. Marginnotes, on the other hand, are marked using superscript numbers such as »[1]«, indicating additional remarks or explanations found at the margin or bottom of the same page. Although rarely used, footnotes can be marked with symbols such as »[*]«.

Declaration of Authorship
The declaration of authorship is printed on the last page of this document.

Contact
For any questions or comments related to this thesis, you are welcome to contact me at:
nikolas.milchers@uni-due.de
As life may take unexpected turns, my private e-mail ensures I remain reachable in the future:
nikolas.milchers@gmail.com

My sincere thanks go to the following people, in no particular order:

Prof. Katrin F. Domke for giving me the opportunity to set up and test the SPM 5500.

Prof. Jochen Stefan Gutmann for kindly serving as the second reviewer of this thesis.

Dr. Detlef Diesing for introducing me to the art of electrochemistry and for becoming a close friend.

Werner Saure for the many constructive and inspiring discussions about electronics we shared while working together and over meals.

Dr. Steffen Franzka for providing samples and for sharing his expertise on both the big picture and the finer details.

My wife Miya for her patience, support, and for enduring life with a scientist.

All of you have helped me grow beyond where I once stood. Thank you.

– Nikolas Milchers

And to those I may have forgotten - thank you as well.

Abstract

In this master's thesis, the Agilent SPM 5500 scanning probe microscope was set up, configured, and systematically evaluated with a particular focus on the implementation of the scanning tunneling microscopy (STM) mode. As a first step, the STM functionality was verified and calibrated using highly oriented pyrolytic graphite (HOPG), providing a reproducible reference system for assessing imaging performance.

Subsequently, electrochemical scanning tunneling microscopy (EC-STM) measurements were carried out on a gold thin-film sample with an initially unknown surface structure. The experiments aimed at investigating potential-induced surface modifications under electrochemical control. While stable and reproducible STM imaging was successfully achieved, limitations were encountered in the electrochemical operation of the SPM 5500. The observed discrepancies between electrochemical measurements performed with the SPM 5500-integrated potentiostat and those obtained using an external AGEF potentiostat suggest that the EC functionality of the SPM 5500 may be impaired.

Furthermore, electrochemical reference measurements were conducted to enable a qualitative comparison between the two potentiostat systems. Although the absolute electrochemical quantities differ significantly, qualitative trends could be identified. Overall, this work demonstrates the reliable operation of the STM mode of the SPM 5500 and provides a methodological basis for future EC-STM studies, while highlighting the need for further validation and potential repair of the integrated electrochemical module.

In addition to characterizing the measurement modes, this work is intended to serve as a practical guide for future studies using the SPM 5500 and to facilitate the introduction of new users to the system.

Zusammenfassung

In dieser Masterarbeit wurde das Rastersondenmikroskop Agilent SPM 5500 aufgebaut, konfiguriert und systematisch hinsichtlich seiner Funktionalität untersucht, mit besonderem Fokus auf die Implementierung des Rastertunnelmikroskopie-Modus (STM). In einem ersten Schritt wurde die STM-Funktionalität anhand von hochorientiertem pyrolytischem Graphit (HOPG) verifiziert und kalibriert, der als reproduzierbares Referenzsystem zur Bewertung der Abbildungsleistung diente.

Anschließend wurden elektrochemische Rastertunnelmikroskopie-Messungen (EC-STM) an einer Gold-Dünnfilmprobe mit zunächst unbekannter Oberflächenstruktur durchgeführt. Ziel dieser Experimente war die Untersuchung potenzialinduzierter Oberflächenmodifikationen unter elektrochemischer Kontrolle. Während stabile und reproduzierbare STM-Aufnahmen erfolgreich erzielt werden konnten, traten Einschränkungen im elektrochemischen Betrieb des SPM 5500 auf. Die beobachteten Abweichungen zwischen elektrochemischen Messungen, die mit dem im SPM 5500 integrierten Potentiostaten durchgeführt wurden, und Referenzmessungen mit einem externen AGEF-Potentiostaten deuten darauf hin, dass die EC-Funktionalität des SPM 5500 möglicherweise beeinträchtigt ist.

Darüber hinaus wurden elektrochemische Vergleichsmessungen durchgeführt, um einen qualitativen Vergleich zwischen den beiden Potentiostatsystemen zu ermöglichen. Die untersuchten elektrochemischen Größen unterscheiden sich deutlich. Insgesamt zeigt diese Arbeit die zuverlässige Funktionsfähigkeit des STM-Modus des SPM 5500 auf und liefert eine methodische Grundlage für zukünftige EC-STM-Studien, während zugleich der Bedarf an weiterer Validierung sowie einer möglichen Instandsetzung des integrierten elektrochemischen Moduls hervorgehoben wird.

Neben der Charakterisierung der Messmodi soll diese Arbeit zudem als praxisorientierte Anleitung für zukünftige Untersuchungen mit dem SPM 5500 dienen und insbesondere Neueinsteigerinnen und Neueinsteigern den Einstieg in die Arbeit mit diesem System erleichtern.

Contents

List of Figures

List of Tables

1 Introduction

This chapter introduces the motivation behind the present work, outlines the underlying problem statement, and summarizes the relevant related work. It provides the conceptual and experimental context for the investigations presented in the subsequent chapters.

1.1 Motivation and Backround

The steadily increasing global demand for energy and the associated reliance on fossil fuels are major drivers of climate change, threatening the quality of life and livelihoods of many people worldwide. The Fukushima reactor accident in 2011[1] acted as a catalyst for comprehensive legislative reforms in Germany, which included, among other measures, the phase-out of nuclear power plants and the accelerated expansion of renewable energy sources[2]. A central element of this energy transition is the production of green hydrogen, which, remains highly energy-intensive, due to its electrochemical production route[3].

New catalysts, tailored through optimized surface properties, have the potential to enhance the efficiency of hydrogen production. Understanding the underlying physical and chemical mechanisms is essential for their development. Electrochemistry provides a powerful framework for studying such surface processes, while scanning tunneling microscopy (STM) enables atomic-scale imaging of catalyst surfaces.

In the long term, the EC-STM mode will be used for in situ structural analysis of surfaces in electrochemically active media. Such investigations offer nanoscale insights into dynamic processes at electrode surfaces and thus make a valuable contribution to the workgroup fundamental electrochemical research.

1.2 Problem Statement and Objectives

The scanning probe microscope (SPM) utilised in this report is an Agilent Technologies 5500 Scanning Probe Microscope (hereinafter referred to as SPM 5500), which was procured in 2016 by the *Max-Planck-Institute for Polymer Research*[4] (hereinafter referred to as MPI-P) in Mainz. Following the appointment of Katrin F. Domke as a professor at the University of Duisburg-Essen[5], the device was transferred to the campus Essen by the company *Kons & Pusnik Umzüge GmbH*[6]. However, at the time of the transfer, there were no employees available who possessed the necessary skills to operate the device. Accordingly, the constituent elements were meticulously cleaned, methodically assembled, and subsequently initiated in accordance with the prescribed guidelines outlined in the Agilent Technologies user's guide[7].

As the main part of this master's thesis, the EC-STM mode (electrochemical scanning tunneling microscopy) of the SPM 5500 was systematically

evaluated with respect to its functionality and applicability. The focus was placed on assessing operational stability, tunneling signal quality, and measurement reproducibility. As the research group is still in stage of development and no established expertise with this instrument was available, this work additionally involved the one person setup, familiarization, and initial operation of the EC-STM system by me.

These investigations build directly on the findings of a previous preliminary study (my Vertiefungsarbeit), in which basic calibrations and initial test measurements were performed in AFM mode using the same instrument.

1.3 Related Work

Although the primary focus of this work lies on the implementation and configuration of the STM mode of the SPM 5500, previous studies serve as a practical point of orientation. In particular, the works of Yoshida *et al.*[8] and Wandlowski *et al.*[9] demonstrate the feasibility of investigating potential-induced structural changes at metal–electrolyte interfaces using EC-STM techniques. These studies therefore provide the general framework for the experiments carried out in the present work. The setup and operation of the SPM 5500 were additionally conducted in accordance with the manufacturer's user manual[7] for the SPM 5500 provided by Agilent.

It should be emphasized, however, that the experimental approaches reported by Yoshida and Wandlowski cannot be reproduced in full within the scope of this study. Limitations in available instrumentation, experimental complexity, and overall effort restrict the degree of reproducibility. Consequently, the experiments presented here are intended as orienting measurements rather than as direct reproductions of the literature results and are discussed accordingly in the Discussion (Section. 6).

[8]: Yoshida et al. (2014), "Reconstruction and Electrochemical Oxidation of Au(110) Surface in 0.1 M H2SO4"

[9]: Wandlowski et al. (2004), "Surface Enhanced Infrared Spectroscopy—Au(11 1-20nm)/Sulphuric Acid—New Aspects and Challenges"

[7]: (2012), *Keysight 5500 Scanning Probe Microscope*

Theoretical Background 2

In science it is crucial to distinguish between physical and chemical processes, as both can be studied and play a significant role in the interpretation of results. Making this distinction requires a precise definition of what constitutes a physical process versus a chemical process.

> Chemie ist die Lehre von den Stoffen und den stofflichen Veränderungen.
> (engl.: Chemistry is the study of substances and material changes.)
>
> Hubert Laitko (1935 - 2024)[10]
> Philosophische Fragen der Chemie[11]

In physical processes, only the external form of a substance changes through the absorption or release of energy. The characteristic (chemical) properties remain unaffected by these processes. Classical physical processes are, for example, deformation, machining, mixing, crushing, separation or a change of aggregate state.
Processes that change the internal properties of a substance are referred to as chemical reactions. New substances with new properties are created in this process.[11]

In physical processes, only the external characteristics of a substance are altered, typically through the absorption or release of energy, while its intrinsic chemical properties remain unchanged. Common examples of physical processes include deformation, machining, mixing, crushing, separation, and changes in the state of matter.

In contrast, chemical processes involve transformations that alter the internal properties of a substance, resulting in the formation of new substances with distinct chemical and physical properties.[11]

The chemical process underlying this work is the electrolysis of water.

$$2\,H_2O(l) \longrightarrow 2\,H_2(g) + O_2(g) \tag{2.1}$$

At room temperature, the liquid reactant water (H_2O) is decomposed into the two gases hydrogen (H_2) and oxygen (O_2) by applying a potential of approximately 1.50 V. The standard potential $E^{\ominus}$ for water splitting is 1.23 V[12, p. 1116]. However, in practical experiments, additional effects increase this potential. This phenomenon is referred to as overpotential.

To investigate such reactions, (electro-) chemistry employs various instruments and techniques. Fundamentally, a potentiostat is used, which, among other applications, can generate cyclic voltammograms.

2.1 Experimental Methods

2.1.1 Scanning Tunneling Microscopy (STM)

Since its introduction in the early 1980s, scanning tunneling microscopy (STM) has become an established technique for the investigation of conductive and semiconductive surfaces with atomic-scale resolution.[13] The method relies on the measurement of a tunneling current between a sharp metallic tip and a sample surface, which occurs when a bias voltage is applied and the tip-sample distance is reduced to the sub-nanometer range. Owing to the strong dependence of the tunneling current on this distance, STM is highly sensitive to changes in surface topography and electronic structure.

In practice, STM measurements are carried out by scanning the tip laterally across the sample surface using piezoelectric actuators while simultaneously recording the tunneling current. A feedback loop continuously adjusts the vertical position of the tip to maintain a defined tunneling condition. The recorded signal is then used to reconstruct an image of the rasterized surface.

A schematic representation of the STM setup and the associated feedback mechanism is shown in Figure 2.1.

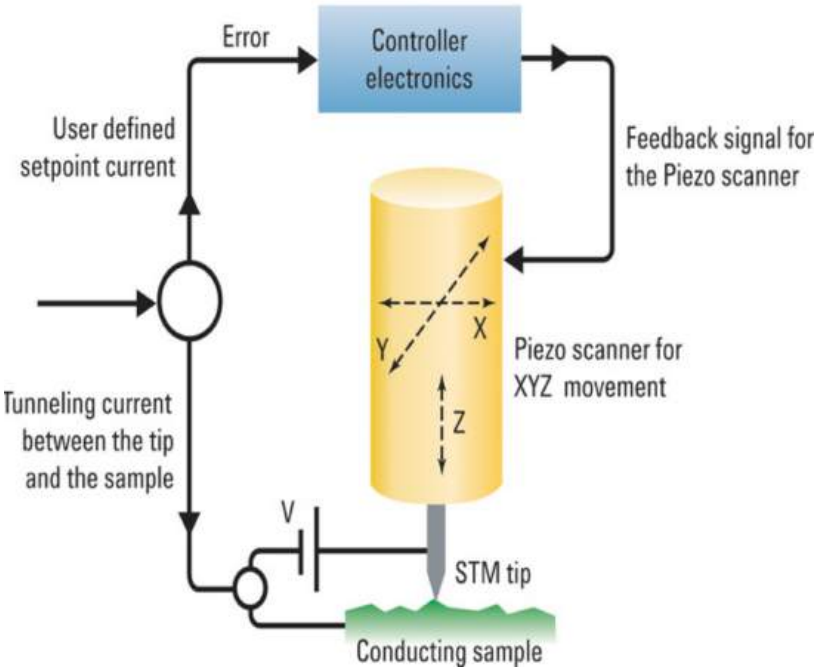

Figure 2.1: Basic STM setup illustrating the main components of the STM system.[7, p. 19]

When STM is operated in an electrochemical environment (electrochemical STM, EC-STM), it enables *in situ* investigation of electrode surfaces under potential control.[7, 14] In this configuration, the STM tip is typically coated with an insulating layer, leaving only the apex exposed to the electrolyte. This design minimizes faradaic currents at the tip and allows stable tunneling conditions in liquid environments.

Compared to measurements in air or vacuum, EC-STM experiments are more sensitive to external influences such as electrolyte composition, temperature, surface contamination, and mechanical stability.

For metallic systems, particularly gold, EC-STM is of special interest. Gold is widely used as an electrochemical working electrode due to its chemical inertness, corrosion resistance, and well-defined surface properties. In addition, gold thin films are commonly employed in electrochemical model systems, making them suitable candidates for EC-STM investigations.[7–9]

STM measurements can be performed in different operational modes. The most commonly used mode is the constant current mode, in which the tunneling current is kept constant by dynamically adjusting the vertical position of the tip via a feedback loop. The resulting height signal $z(x, y)$ is recorded and used to generate an image of the surface. It should be noted that the obtained contrast reflects a convolution of geometric topography and local electronic properties, such as variations in the local density of states.[7]

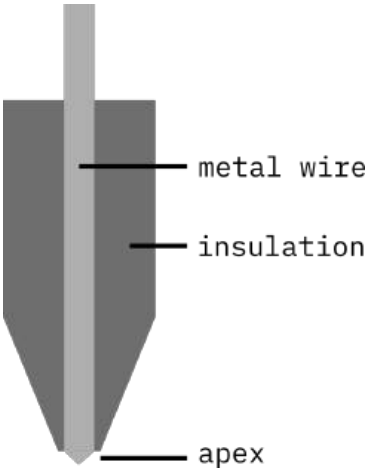

Figure 2.2: Schematic cross section of an insulated STM tip used for measurements in aqueous electrolyte environments similar to KEYSIGHT N9802A-GF tips (see 3.1).

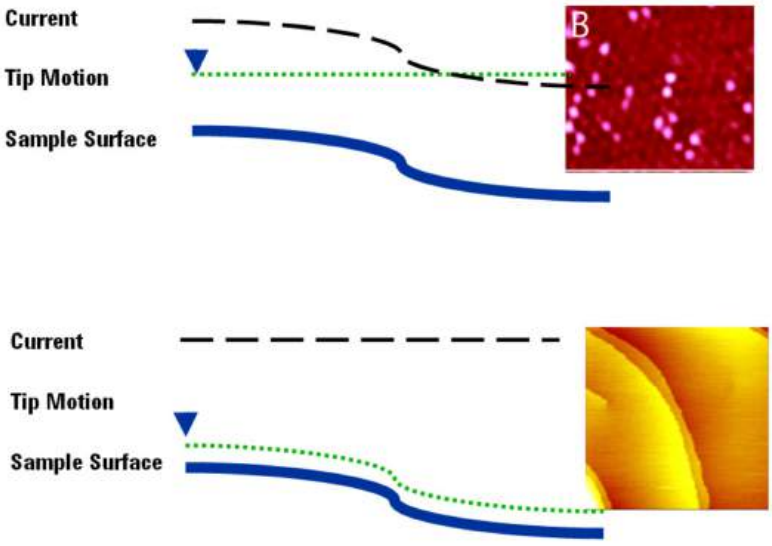

Figure 2.3: Comparison of STM operation modes. Constant height mode (top) enables faster imaging but is limited to smooth surfaces, whereas constant current mode (bottom) allows mapping of larger variations in the vertical (z) direction.[7, p. 20]

Alternatively, STM can be operated in constant height mode, where the tip height is fixed and variations in the tunneling current are recorded directly. While this mode allows faster data acquisition due to the absence of feedback response, it requires very flat and well-defined surfaces to avoid tip-sample contact. In addition, scanning tunneling spectroscopy (STS) can be performed by varying the bias voltage at a fixed lateral position, providing information on the local electronic structure of the sample.[13]

Within the scope of this work, STM measurements were exclusively carried out in constant current mode, as this mode provides the highest operational stability for electrochemical experiments and rough or inhomogeneous thin-film surfaces.[7, p. 20]

2.1.2 Cyclic Voltammetry

Cyclic voltammetry (CV) is a versatile and indispensable technique in electrochemistry, providing both qualitative and quantitative insights into redox processes, reaction mechanisms, and the electrochemical properties

of materials and surfaces. By applying a linearly swept potential that reverses direction at defined limits (this area with a lower and upper potential limit is called potaential window), CV facilitates the analysis of redox-active species and their dynamic behavior in specific chemical environments. This makes it particularly valuable for studying and characterizing electrochemical systems such as batteries, biochemical processes, and catalytic reactions. Cyclic voltammograms yield critical information on reaction reversibility, the number of electrons involved in redox transitions, and the overall reaction kinetics, establishing CV as a tool across various research disciplines.

Globally, two formats for presenting cyclic voltammograms are commonly used: the IUPAC (International Union of Pure and Applied Chemistry) and the US standards (Unified Conditions), which differ in the orientation of the x- and y-axes[15] (see Fig. 2.4).

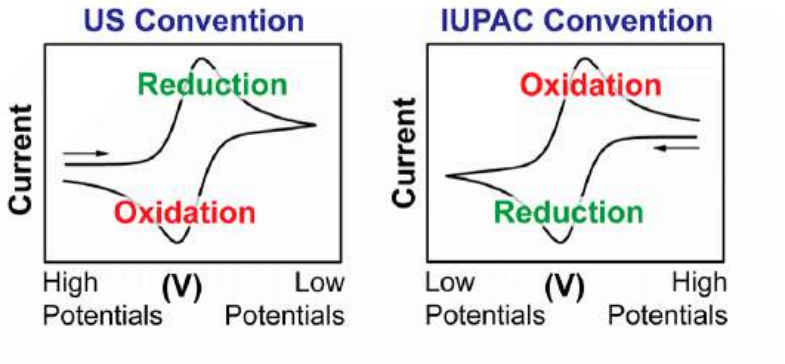

Figure 2.4: Two conventions are commonly used worldwide for representing cyclic voltammograms (CVs). In the so-called U.S. convention, the current is plotted on the y-axis, while the potential on the x-axis decreases from more positive to more negative values. In contrast, the IUPAC convention also plots the current on the y-axis but displays the potential on the x-axis increasing from lower to higher values.[15]

The difference between the two conventions arises from a horizontal mirroring of the cyclic voltammograms, which effectively exchanges the reduction and oxidation regions. As a result, the plots appear rotated by 180° (see Figure 2.4).

The potential is often reported against standard reference electrodes such as the Standard Hydrogen Electrode (SHE), Ag/AgCl, or Saturated Calomel Electrode (SCE), with conversions provided if required. In this work the used reference electrode will be a Pt-H electrode.

2.1.3 Potentiostat

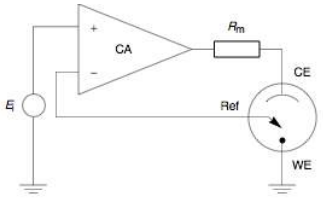

Figure 2.5: Simplified schematic representation of a potentiostat based on an operational amplifier (CA) and a three-electrode electrochemical cell consisting of a reference electrode (RE), working electrode (WE), and counter electrode (CE).[16]

A potentiostat is a fundamental instrument in electrochemical research, designed to control and measure the electrical parameters of an three electrode electrochemical cell. Its primary function is to maintain a constant potential difference between the working electrode (WE) and the reference electrode (RE), enabling the investigation of various electrochemical processes such as redox reactions, corrosion, and electrodeposition.[16]

The WE is the component of the electrochemical cell under study, while the RE serves as a stable reference point for potential measurement. The CE completes the electrical circuit and compensates for the current flowing through the WE. By the nature of the system, the CE facilitates reactions opposite to those occurring at the WE. However, since the WE typically has a significantly smaller surface area compared to the CE, it serves as the limiting factor for electron flow and, consequently,

for the electrochemical reactions. By applying a controlled potential to the WE relative to the RE, the potentiostat allows researchers to probe the electrochemical behavior of materials or solutions with minimal interference from the electrode itself.[17]

In operation, the potentiostat continuously adjusts the potential passing through the CE to maintain the desired potential at a specific time at the WE. This feedback mechanism ensures that the set potential is controlled, even as the electrochemical reactions alter the systems conditions. Simultaneously, a *storage* oscilloscope is connected to the potentiostat and records the current response of the WE. The signal detected which is directly related to the electrochemical activity occurring at the electrode surface. The data obtained from potentiostatic measurements, such as current-voltage relationships, provide critical insights into reaction kinetics, diffusion processes, and material properties.

A potential-time diagram with a corresponding current-time response can be transformed into a potential-current diagram. These resulting plots are referred to as cyclic voltammograms, which form the basis of cyclic voltammetry.

Equipment and Instruments 3

This section introduces the main experimental equipment used to obtain the results presented in Chapter 5. Both the individual instruments and auxiliary tools requiring particular attention are described. The section concludes with an overview of the software employed; where available as open-source software, the corresponding packages are provided in the digital appendix of this work.

3.1 Potentiostats

Agilent Technologies 5500 Scanning Probe Microscope

The primary experimental setup used in this work is the Agilent Technologies 5500 Scanning Probe Microscope (SPM) (see fig. 3.1a and 3.1b), which can be operated in various AFM and STM modes using interchangeable scanner heads. For the present study, the STM scanner head (model N9501A, option 001) was employed in combination with coated Pt-Ir- STM tips (N9802A). The instrument is equipped with an integrated potentiostat, enabling the combination of electrochemical experiments with STM measurements.

Such EC-STM measurements can be performed either under dynamic conditions, where the potential in the electrochemical cell is varied during STM imaging, or under static conditions, where a fixed potential is applied. In the present work, STM measurements were conducted at several defined static potentials.

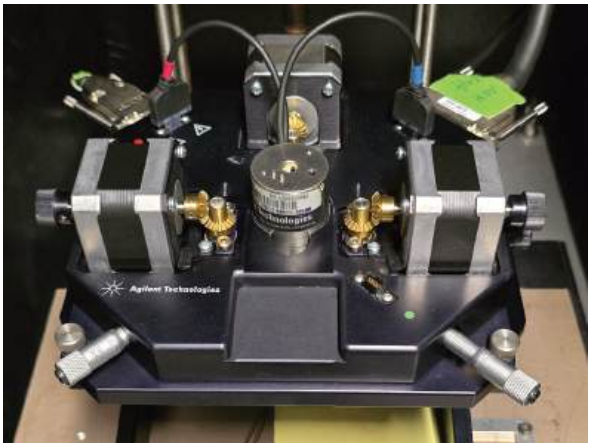

(a) SPM 5500 scanner with stepper motors mounted on a holding frame and an inserted STM head.

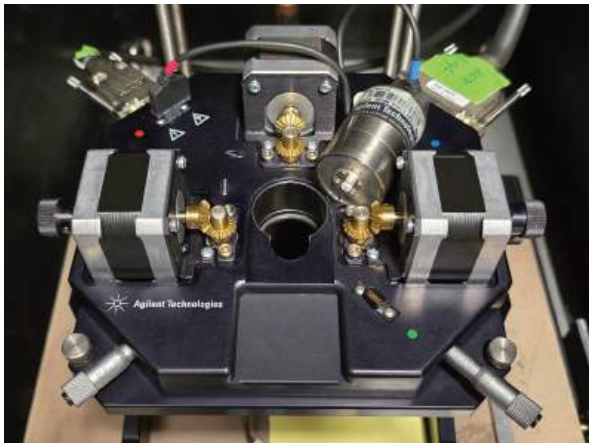

(b) SPM 5500 scanner with stepper motors mounted on a holding frame. The connected but not clamped STM scan head is positioned between two stepper motors. An inserted tip, here a coated Agilent Pt-Ir tip, is shown.

Figure 3.1: Comparison of detailed views of the SPM 5500 scanner mount with the inserted STM head and the removed STM head.

The SPM 5500 scanner is designed such that the measurement head is inserted into the instrument from above, while the sample holder (see

fig. 3.8) is magnetically attached from below.[7, p. 99] Three stepper motors are used to approach the sample towards the scanner head under software control. Lateral positioning of the sample during coarse approach is performed manually using two silver micrometer screws located on the left and right front sides of the scanner. This configuration provides a high degree of flexibility at the expense of positioning accuracy.

Figure 3.2: SPM controller, HEB (electronics head box), control computer (old and new), as well as the SPM components for AFM measurements in a 19-inch laboratory rack.

Due to the instrument design, particularly in STM mode, no digital visual assistance (e.g., camera-based guidance) is available. This represents a limitation, as regions of interest on the sample surface must be approached blindly. Consequently, relocating a previously imaged area is practically not possible.

In addition to wear-related play in the micrometer screws resulting from prolonged use, the scanner head itself does not have a fixed orientation within its holder. Owing to its circular geometry and the slightly off-center position of the STM tip, reliable and reproducible alignment is not inherently ensured. To mitigate this effect, small reference marks were recently added to the scanner head using a red marker. These markings do not affect the measurements but ensure that the scanner head is inserted in a consistent orientation.

Control of the STM 5500 is handled by the system controller in combination with the HEB (head electronic box) unit.[7, p. 305] The acquired data are transmitted to a dedicated PC, where they are stored and processed using the associated software (see Section 3.2). The equipment rack housing the individual components is shown in Figure 3.2.

For the STM measurements, commercially available KEYSIGHT N9802A-GF tips were used. The package employed at the beginning of this work was unopened. These tips are specifically designed for use in aqueous electrolyte solutions. Once a tip is considered spent, the insulating coating can be removed using a scalpel to expose the Pt-Ir wire. The tip can then be re-cut with a blade and reused for measurements in air, for example for STM calibration on highly oriented pyrolytic graphite (HOPG).

AGEF Potentiostat

1: Google Scholar Profile Detlef Diesing

2: Link to the AGEF hompage

In order to compare the electrochemical data of the SPM 5500, the in-house AGEF potentiostat was used. No data sheet is available, but it was built in 1993 by Martin Schramm and Detlef Diesing[1] as part of the AGEF[2] (*Arbeitsgemsinschaft elektrochemischer Forschungsinstitutionen e.V.*).

The potentiostat was provided by Detlef Diesing. Since this potentiostat is used for many basic experiments in the advanced practical course in physical chemistry at the University of Duisburg-Essen, and the data is compared with literature, it can be assumed that it functions without error.

In contrast to the potentiostat integrated into the Agilent SPM 5500, the external AGEF potentiostat generates a continuous, non-digitized potential waveform, which is adjusted to different set values between individual measurements.

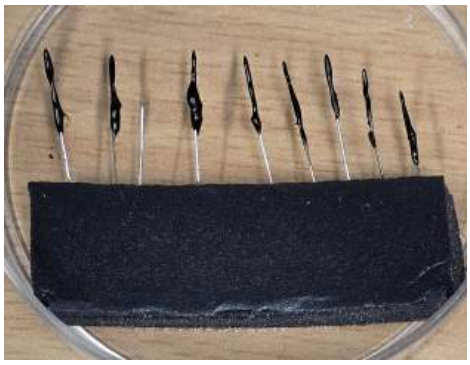

(a) Opened package containing black-insulated STM tips. One tip with an exposed apex is visible (third from the right), identifiable by the silver-colored wire.

(b) Closed STM tip storage case labeled by Keysight. A rubber band can be used to ensure that the case remains securely closed during storage or transport.

Figure 3.3: Coated Keysight STM tips stored with the scanner-insertion side embedded in foam to protect the sensitive tip apex from mechanical damage during storage and transport.

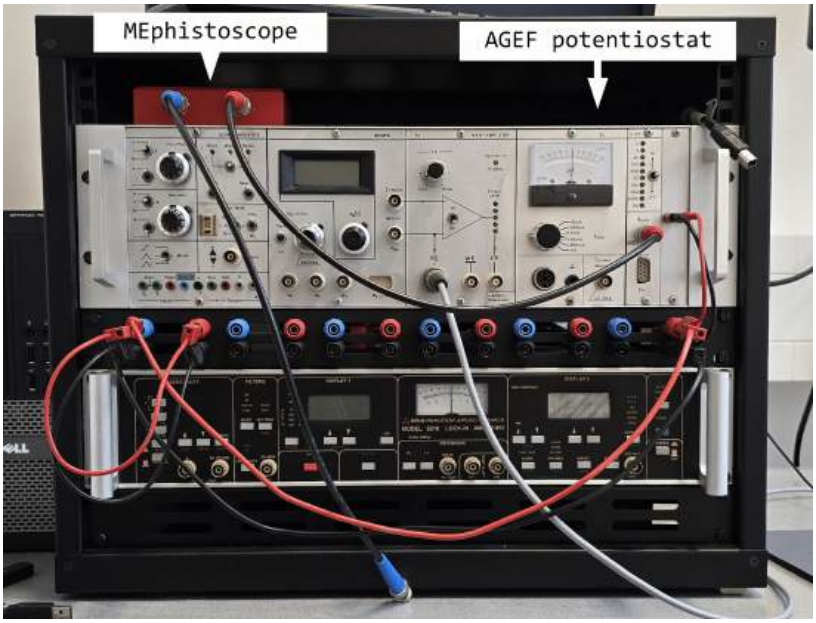

Figure 3.4: Small 19-inch laboratory rack housing the MephistoScope (red unit), the AGEF potentiostat (silver unit in the center), and a lock-in amplifier (black unit at the bottom), which was not used in this work.

The data produced by the AGEF potentiostat is collected by a MEphisto-Scope (see 3.5).

MEphistoScope

The MephistoScope (UM202/UM203) by Meilhaus is a modular 16-bit digital storage oscilloscope designed for time-resolved acquisition of electrical signals. It can be operated either as a conventional oscilloscope or in data-logging mode, allowing continuous recording over extended time periods, (only) depending on computer storage. The system is particularly suited for monitoring slowly varying signals, as commonly encountered in electrochemical experiments. In this work, the MephistoScope was primarily used in data-logging mode to record electrochemical signals.

Figure 3.5: Manufacturer's promotional image of the MephistoScope (Meilhaus Electronic) used in this study. [18]

3.2 Software Tools

In this section, the software employed in this work is presented. The software packages are summarized in Table 3.1, with more detailed descriptions provided in the subsequent sections.

Table 3.1: Overview of Software Tools used.

Software	Version	Purpose
IGOR PRO	9.0.5.1 (Build 56551)	Data analysis, math evaluation
PicoView	1.20.3	STM control, CV acquisition
MEphisto Lab	MEphisto Scope 1 (UM20x)	Data acquisition

IGOR PRO 9

IGOR Pro® is a scientific data analysis and visualization software by WaveMetrics® used for data processing, numerical analysis, and figure generation. In this work, it was employed for data evaluation, fitting procedures, and the preparation of high quality plots.
Unless otherwise stated, the mathematical evaluation of the data is performed using `IGOR PRO Version: 9.0.5.1 (Build 56551)` or newer.

PicoView 1.20.3

PicoView is the all-in-one solution for controlling the Agilent SPM 5500 and for data acquisition with this microscope. The programme is available free of charge at and can also be used without a microscope. A copy of this programme can be found in the digital appendix to this thesis.

Unless otherwise stated, the STM images were captured using `PicoView version 1.20.3` from Keysight Technologies 2016.

This programme was also used to record data various CVs regarding the SPM 5500.

MEphisto Lab

MEphistoLab is the software used to operate the MephistoScope digital storage oscilloscope by Meilhaus ELectronic. The version employed in this work is an earlier release (version 1), which is characterized by its simplicity and operational stability. The software is compatible with operating systems up to Windows 7; installation is no longer supported on newer Windows 10 (or even Windows 11) versions. The corresponding user manual and data sheet is available for download.[3]

3: Website of Meilhaus Electronic.

Using MePhistoLab, the MephistoScope can be operated either as a digital storage oscilloscope or as a data logger. In the present work, the software was exclusively used in its data-logging mode.

3.3 Sample and Sample Preparation

As the initial sample for this work, a 30 nm thick gold thin film was used. To promote adhesion on a silicon wafer with unknown properties, a 9 nm thick titanium layer was deposited (Fig. 3.6).

The sample was fabricated for the University Hospital Essen on 2021-01-24, and kindly provided by Dr. Steffen Franzka. One section with the lateral dimensions 0.52 cm, 0.74 cm, 0.55 cm and 0.97 cm, resulting in a macroscopic surface area of 0.44 cm^2 (Fig. 3.6) was mounted onto a specimen holder (TED PELLA, INC., Prod. No. 16218) to ensure easier handling. The specimen holder, was employed (Fig. 3.7), which had been roughly cleaned of its oxide layer using steel wool. Conductive silver paint (Ferro GmbH, Art. No.: 530042) was used both as an adhesive and later as a contact to the potentiostat; it also directly contacted the gold at the corner with the acute angle.

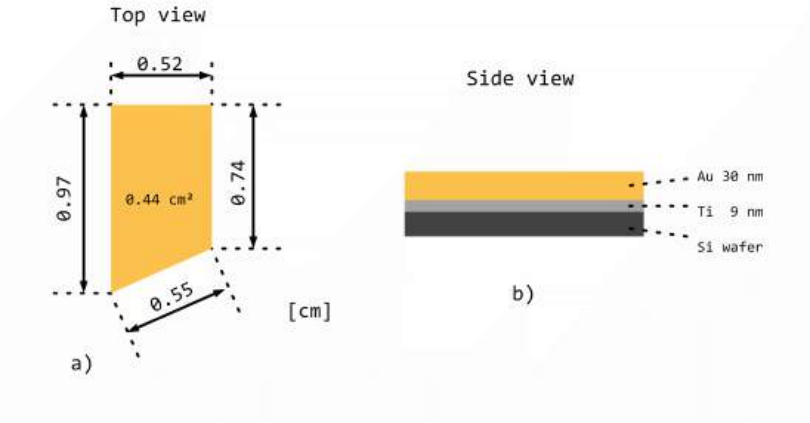

Figure 3.6: Schematic top view (a) and side view (b) of the Au-Ti samples with the assigned dimensions for the University Hospital Essen. The gold film is shown in yellow, titanium as the adhesion-promoting layer in gray, and the Si wafer in dark gray. The AFM sample holder was omitted in this representation.

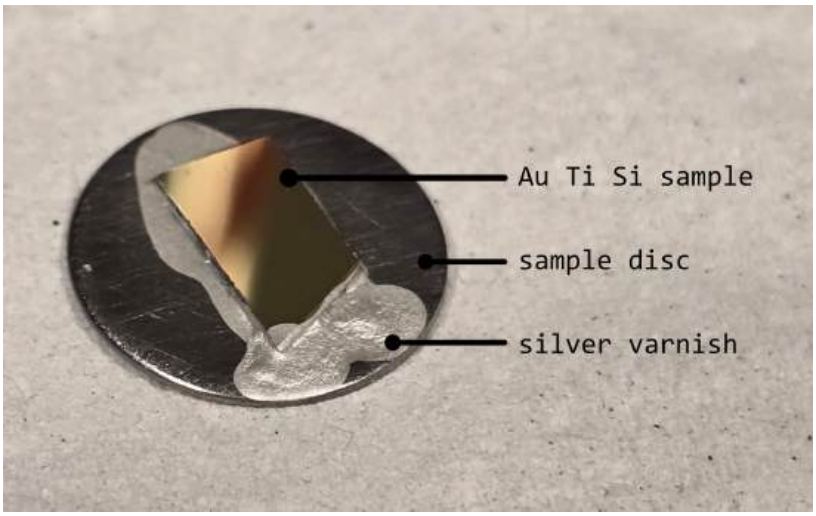

Figure 3.7: Photograph of the freshly deposited gold sample mounted on the sample holder with drying silver conductive paint.

Due to the magnetic specimen disc, the sample can be mounted onto the magnetic sample holder of the SPM 5500. According to the description in the SPM 5500 user manual, the CE, RE, and the tungsten contact arc are clamped between the white block and the metal spring loaded contact screws.[7, p. 138] The setup deviates from the experimental arrangement proposed by Keysight, since the sample itself is too small to be placed into the liquid cell (see fig. 3.8).

The experimental setup is modified in such a way that the electrochemistry takes place between a droplet and the gold surface, rather than between the gold surface and a larger liquid volume (see fig. 3.9). During the experiment, care must be taken to ensure that the droplet does not evaporate.

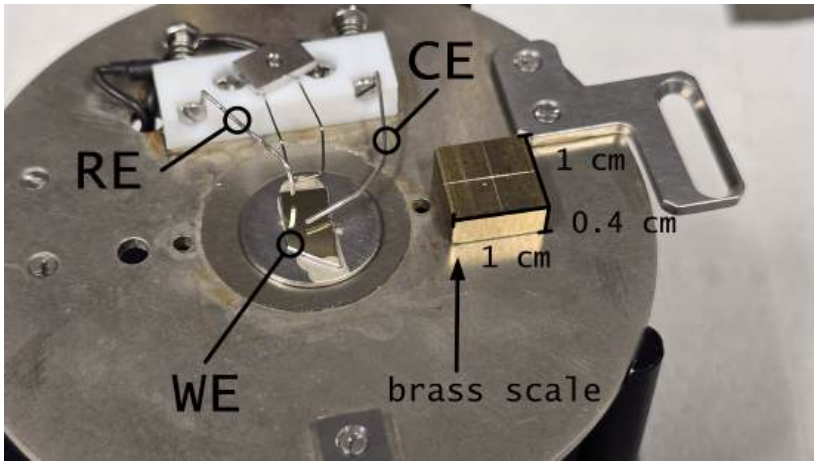

Figure 3.8: Mounted specimen holder with sample, magnetically fixed and contacted by a tungsten arc, with inserted Pt-CE and RE without electrolyte. To provide a better representation of the dimensions, a brass scale bar with the dimensions H×W×D (0.4 cm × 1 cm × 1 cm) was placed on the specimen holder.

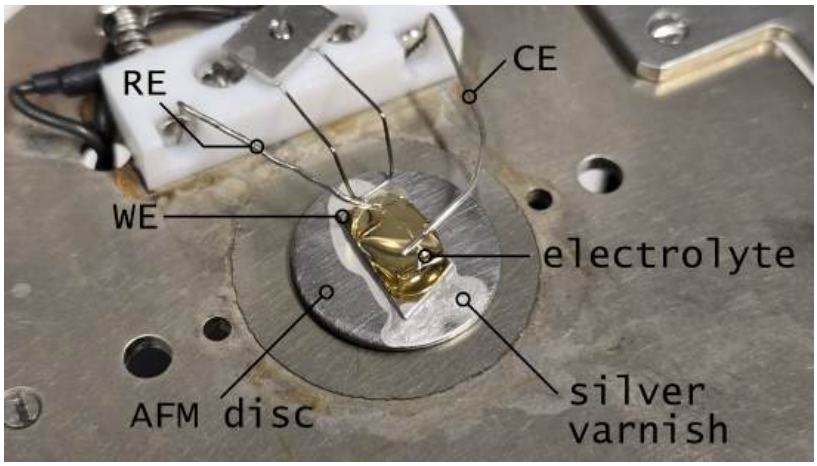

Figure 3.9: Close-up of the cell prepared for the experiment with electrolyte droplet and inserted electrodes shortly before insertion into the multipurpose scanner of the SPM 5500.

Prior to the experiment, the electrical contact between the sample and the contacts to the SPM 5500 is verified using a multimeter in continuity mode.

Using the software PicoView 1.20.3[19], the STM function is employed to establish contact between the tip and the sample surface, as well as to acquire the actual STM images. The EC function is also controlled via the software. With the corresponding parameters, the following experiments (see Chapter 5) can then be performed.[7, p. 114 ff., 216 ff.]

The prepared cell was then connected to the potentiostat of the SPM 5500 via a cable and inserted into the scanner using the magnetic holder.

3.4 Electrolyte Preparation

The same electrolyte solution was used for all experiments conducted in this work. Following the approach of Yoshida *et al.* and Wandlowski *et al.*, a 0.1 mol L^{-1} H_2SO_4 solution[8, 9] was employed. As only small

volumes were required during the experiments—electrolyte droplets for the measurements and a few milliliters for preparation of the reference electrode—a total volume of 100 mL was prepared.

The electrolyte was prepared using 95 % sulfuric acid (VWR, NORMAPUR grade, lot 22H104011, Art. No. 20700.320) as the stock solution. A concentration of 95 % H_2SO_4 corresponds to 17.76 mol L^{-1}.[20, chapter 7.1.3.2] Accordingly, 563 µL of the stock solution were diluted in room temperature to a final volume of 100 mL to obtain a 0.1 mol L^{-1} H_2SO_4 solution (see calculation 3.1).

$$\begin{aligned} c_1 \cdot V_1 &= c_2 \cdot V_2 \\ 17.76\,\mathrm{mol/L} \cdot V_1 &= 0.1\,\mathrm{mol/L} \cdot 100\,\mathrm{mL} \\ V_1 &= \frac{0.1\,\mathrm{mol/L} \cdot 100\,\mathrm{mL}}{17.76\,\mathrm{mol/L}} = 0.563\,\mathrm{mL} = \underline{\underline{563\,\mu\mathrm{L}}} \end{aligned} \tag{3.1}$$

The calculated volume was transferred by using an Eppendorf Research pipette (serial no. 3362872). The 100 mL volumetric flask had been previously boiled with Milli-Q water 3x for 10 min.

Calibration and Environmental Data

4

4.1 Calibration of the STM with HOPG

Highly oriented pyrolytic graphite (HOPG) is particularly well suited for the calibration of STM microscopes due to its regular and well-documented hexagonal structure in the literature.[21]

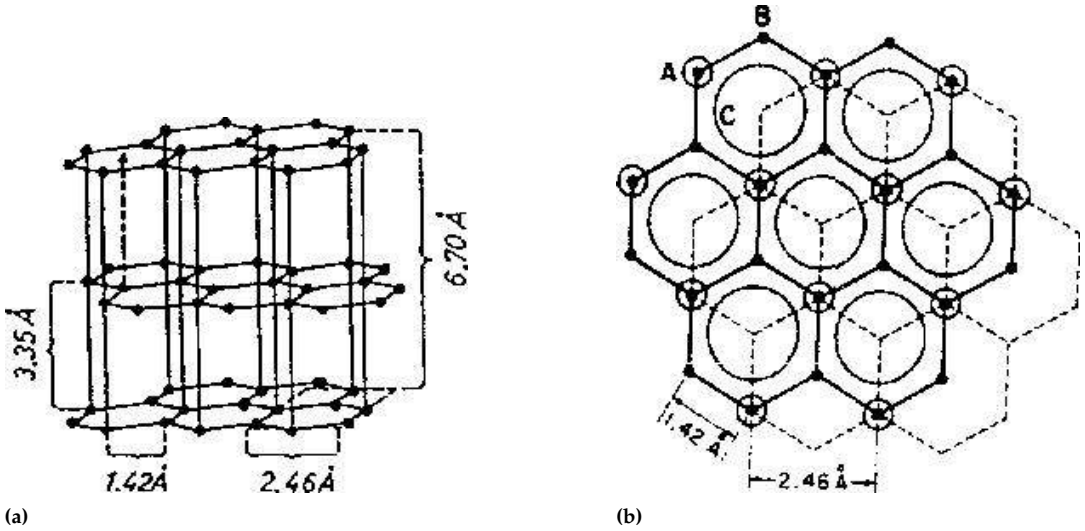

Figure 4.1: (a) Layer structure of HOPG (described by Winzer [22]); (b) nonequivalent α (A) and β (B) lattice sites on the graphite (0001) surface. The dots represent the carbon atoms of the top layer, while the circles indicate those of the underlying layer.[21, 23, 24]

When evaluating the microscopy images, it is important to note a characteristic feature of HOPG: in STM images at the atomic scale, only every second atom of the hexagonal lattice is resolved. This effect is well documented in the literature and is attributed to the electronic structure of graphite.[21]

In STM images, therefore, only one of the two sublattices of the hexagonal honeycomb structure becomes visible (cf. Fig. 4.1 and Fig. 4.4). Tómanek et al. explain this by a pronounced asymmetry in the local density of states at the Fermi energy between α and β lattice sites. The α atoms possess directly orthogonal neighboring carbon atoms (cf. Fig. 4.1a), whereas the β atoms contribute more strongly to the tunneling current.[25]

Preparing HOPG for imaging is straightforward. A sheet of the material is glued onto a specimen disc. The top layer of the HOPG is removed by applying Scotch Tape and carefully peeling off the first layer. The cleaned and renewed surface is then ready for rasterization by the STM tip. The HOPG sample was kindly provided by Dr. Steffen Franzka. It is a well-known sample that has also been used in his measurements and calibration procedures.

With the uncalibrated STM, images were acquired, including Fig. 4.2.

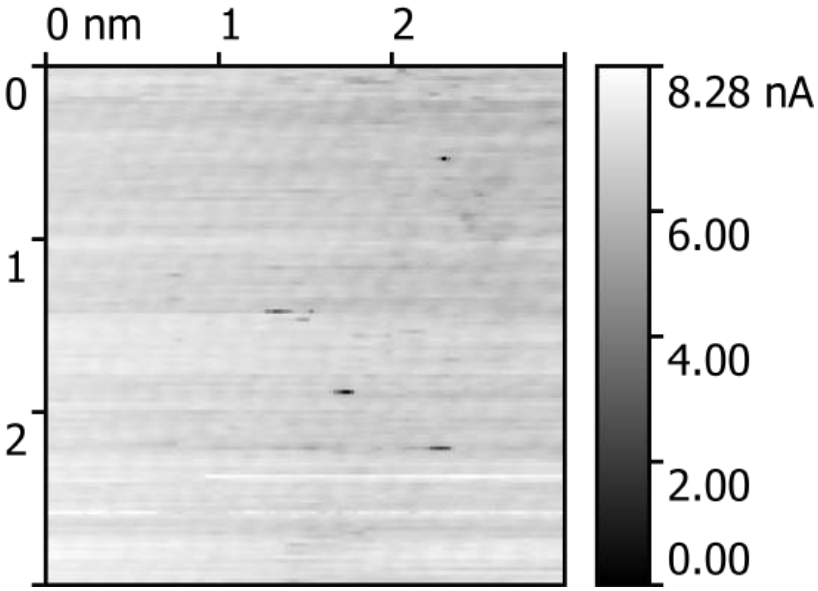

Figure 4.2: STM image of the uncalibrated HOPG sample. 3×3 nm by 128×128 dots, 21 lines per second, acquired with PicoView and analyzed using Gwyddion. Fast scan: x-axis, slow scan: y-axis. Constant-height mode with a detected tunneling current of 0–8.28 nA.
The black spots in the scan are attributed to electronic artifacts and surface contamination. The scan head had been stored for an unspecified period of time, and the image quality improved with continued use.

To enhance and analyze the surface patterns, a two-dimensional Fourier transformation (2D FFT) is performed in Gwyddion (cf. Fig. 4.3a). By selecting the individual atoms, the mask shown in Fig. 4.3b is generated, which highlights the characteristic honeycomb pattern of HOPG (cf. Fig. 4.5).

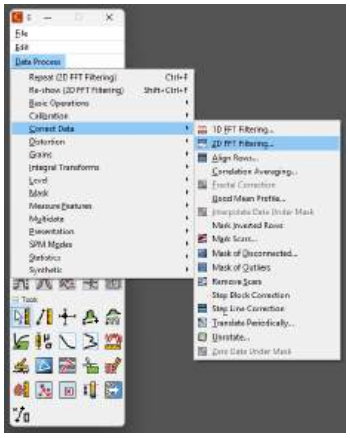

(a) Screenshot of the menu tree for selecting the 2D FFT filtering command in Gwyddion.

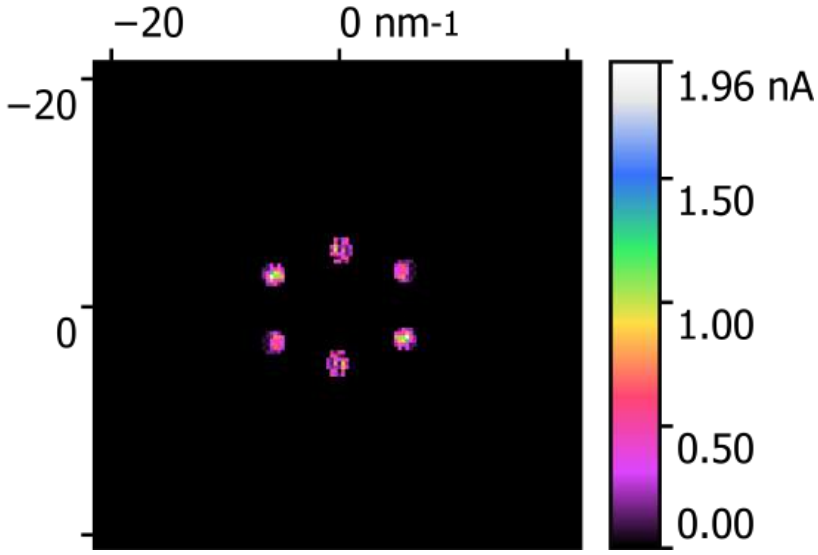

(b) This image shows the mask for the two-dimensional Fourier transformation of Fig. 4.2. The six atoms of a carbon ring were selected to enable a more precise evaluation of Fig. 4.2, resulting in Fig. 4.5.

From the newly obtained Fig. 4.5, the interatomic distances are determined using the profile tool (cf. Fig. 4.1). As mentioned at the beginning of this section, it is important to ensure that the correct hexagonal structure is chosen (marked in red in Fig. 4.4).

The data extracted from the profile are evaluated according to their distances. From 13 measurements, an average spacing of 0.174 ± 0.012 nm $\equiv 1.74 \pm 0.12$ Å was obtained. This deviates from the literature value of 2.46 Å[21] by a factor of 1.41. This correction factor is applied to the

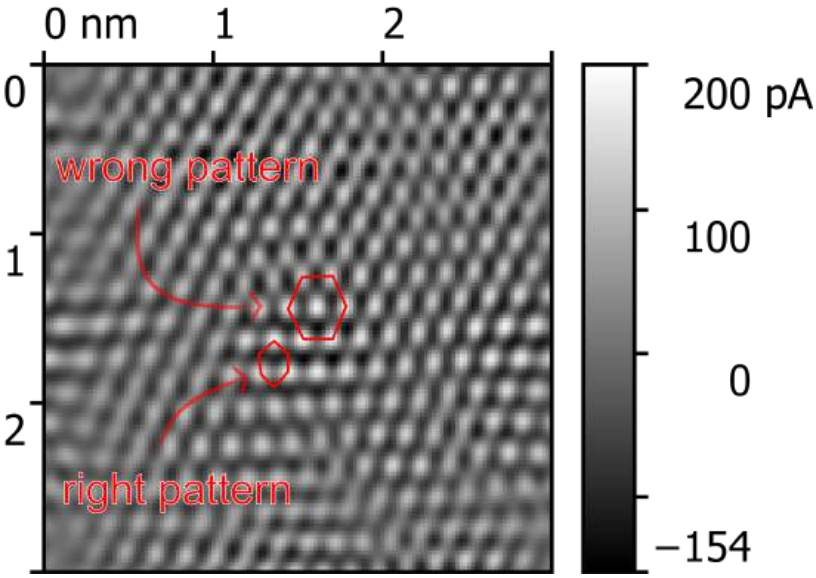

Figure 4.4: Edited representation of the honeycomb structure with the positions of the hexagonal lattice of HOPG indicated.

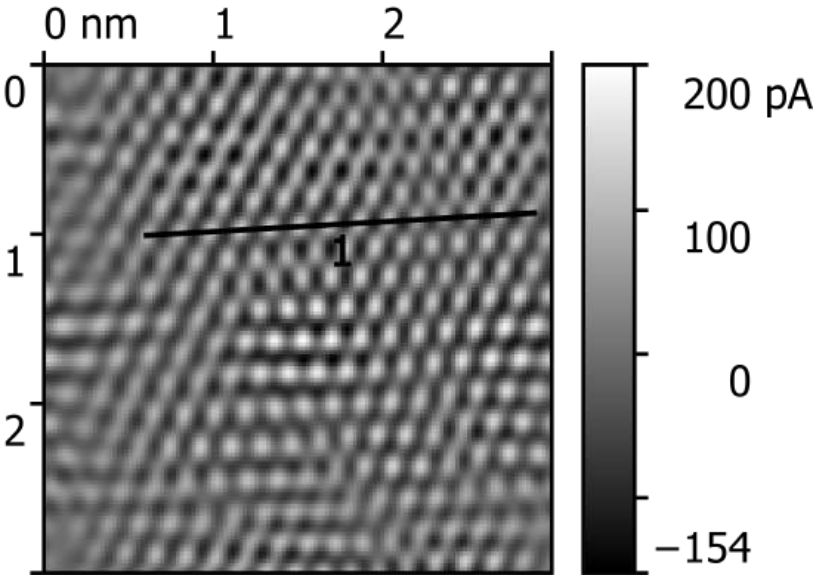

Figure 4.5: Edited representation of the honeycomb structure with the marking of profile (1) for the determination of the distance between two carbon atoms.

sensitivity value stored in PicoView.

Example

The measurement shown in Fig. 4.2 was performed with a preset sensitivity of 250 nm/V. Since the measured distances are smaller by a factor of 1.4, this results in a new sensitivity value of 353 nm/V, which is then entered as the updated sensitivity for the x-coordinate.

To complete the calibration, the described procedure is repeated for the y- and z-coordinates.

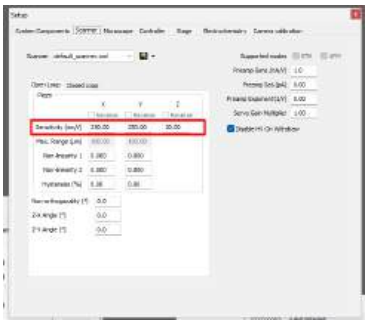

Figure 4.6: Marked in red are the default settings for the sensitivity in PivoView 1.20.3 with a value of 250 nm/V for the x-axis, 250 nm/V for the y-axis and 20 for the z-axis. Every single values has to be corrected by measuring and comparing to literature.

An additional attempt to calibrate the system using a MoS_2 sample was conducted but did not yield reliable results. In contrast, calibration using HOPG proved to be robust and highly reproducible for the SPM 5500. HOPG therefore represents a suitable reference material for learning the fundamental handling of the system, while also providing an effi-

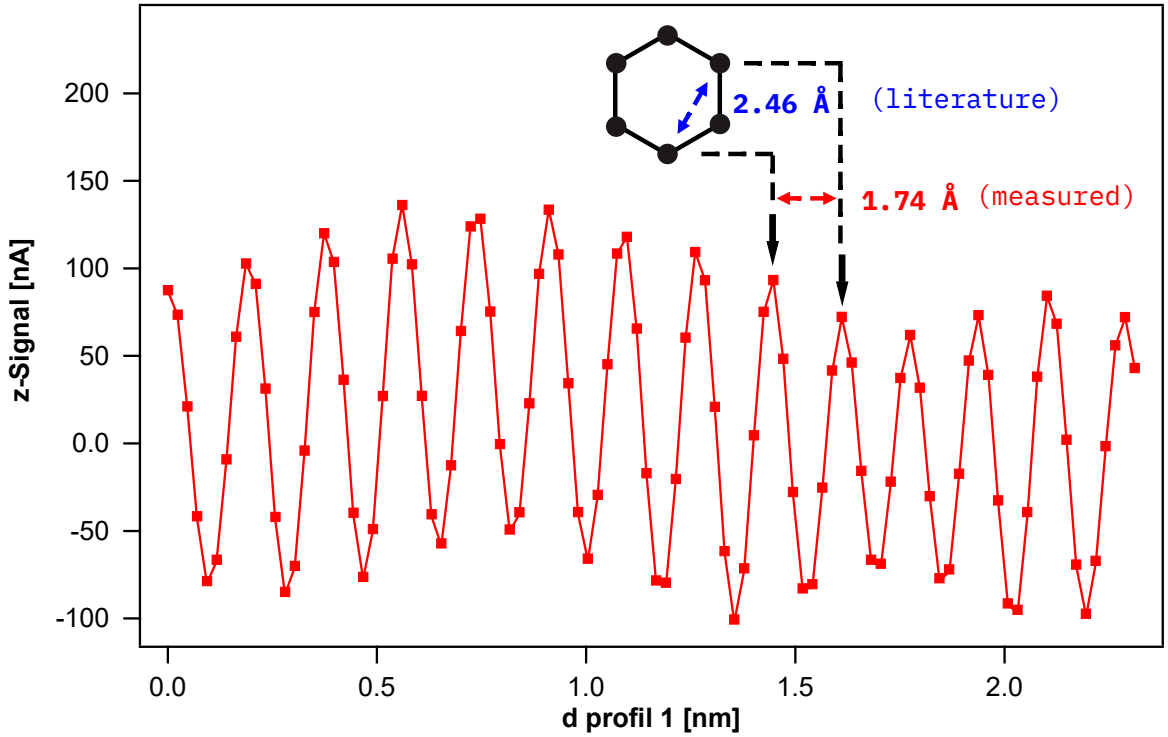

Figure 4.7: This graph shows the extracted *z*-values along the profile 1 from Fig. 4.5. Thirteen atomic sites were captured in this line to calibrate the *x*-axis. The measured values are shown in red, while the schematic hexagonal structure of HOPG is depicted in black. Additionally, the literature value for the distance between the two compared carbon atoms is included.

cient and reliable means for experienced users to monitor instrument performance.

4.2 Environmental data

The user manual specifies the environmental conditions under which the SPM 5500, and thus also the STM mode, operates optimally.[7, p. 4] Compliance with these specifications must be ensured. In addition, stable measurement conditions lead to more reproducible results.
To determine the stability of the environmental conditions, a temperature and humidity two EL-USB-2 data loggers[1] were used to record the laboratory environment over 18 days in 2-minute intervals, as well as that of the neighboring office, which serves as the main access route to the laboratory, in order to enable a comparison.

1: Type: RH / TEMP DATA LOGGER
Software: EasyLog USB Version 7.7.0.0

The sensitivity of the data loggers is limited to 0.5 °C for the temperature and 0.5 % for the humidity. The measurements were carried out in spring 2025, starting at 13:00 without ruinning air conditioning. The sensor for the office data was placed on a desk near a window, next to the computer keyboard. The STM lab sensor was placed next to the vibration reducing chamber, housing the STM, (not inside the chamber!). The collected data for temperatures and humidities were processed in IGOR and are presented in Figs. 4.8, 4.9, and 4.10.

For clarity, all recorded data points are plotted in Fig. 4.8. Since the data density of the red temperature curves and the blue humidity curves is

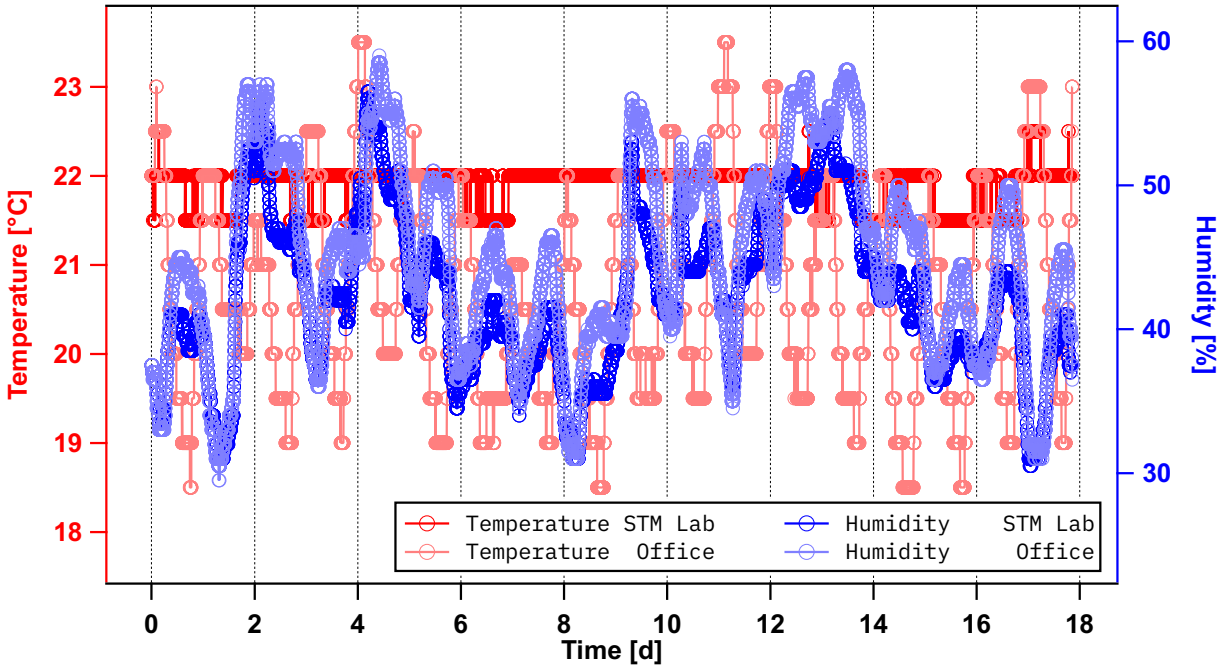

Figure 4.8: This graph shows the collected data for temperature (red) and humidity (blue) from the office (faded red/blue) and the STM laboratory (red/blue). The figure provides an overview of all collected raw data over 18 days. Circles as markers are used for graphical purposes; no error bars are included in this particular graphic.

very high, they are plotted separately in Figs. 4.9 and 4.10, where they are discussed in detail. The results obtained from processing the graphs are summarized in Table 4.1.

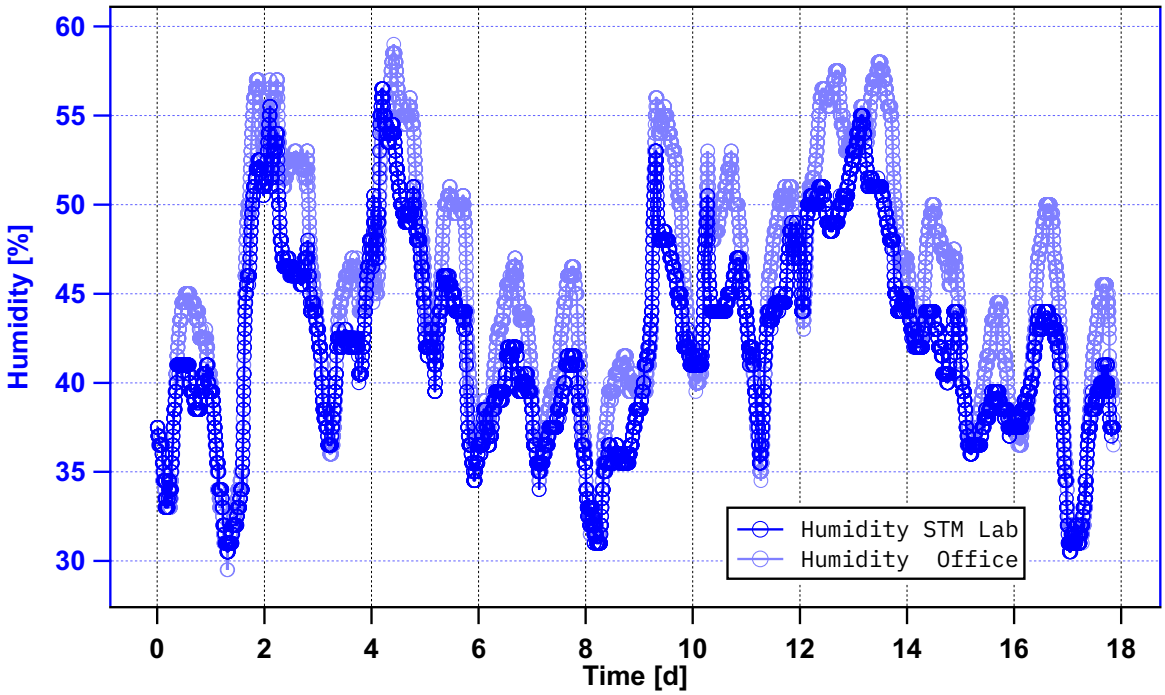

Figure 4.9: This graph shows the humidity data in the office and the laboratory over a period of 18 days. The light blue markers indicate the humidity in the office, while the blue markers indicate the humidity in the STM laboratory.

The humidity trends in the office (light blue) and in the laboratory (blue)

show qualitative similarity. Fluctuations of up to 29.5±0.5 % humidity were measured in the office, while fluctuations in the laboratory reached a maximum difference of 26.0±0.5 %, thus being slightly more stable. Over the entire measurement period, both humidity levels were within approximately the same range.

The dashed lines, orthogonal to the x-axis, indicate 13:00 on the corresponding days. Humidity tends to decrease around midday (between 12:00 and 14:00) and increase again in the evening. This can be explained by the daily temperature variations (cf. Fig. 4.10), since warm air can absorb more moisture, resulting in lower relative humidity for the same absolute water content.

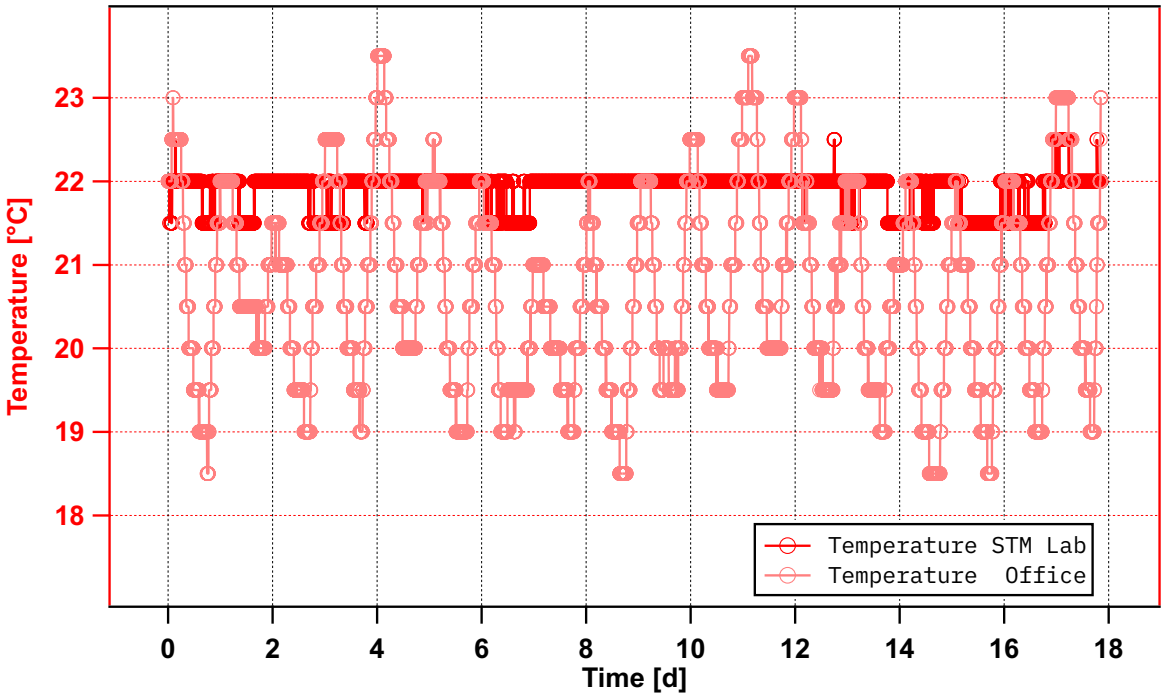

Figure 4.10: This graph shows the detected temperature data in the office and the laboratory over a period of 18 days. The light red markers indicate the air temperature in the office, while the blue markers indicate the temperature in the STM laboratory.

In contrast to the fluctuations in humidity, the temperature variations differ both qualitatively and quantitatively. The temperature in the laboratory is constant within the accuracy of the data logger. The values oscillate between 21.5 °C and 22.0 °C, which corresponds exactly to the resolution of the measuring instrument (ΔT = 0.5 °C and Δrh = 0.5 %). The office temperature, by contrast, exhibits the typical daily cycle with a maximum around midday and a local minimum at night (cf. Fig. 4.11, e.g., at 4.6 d and 5.6 d).

The key findings, such as the average humidity and temperature at the respective locations, as well as the specifications provided by Agilent for the SPM 5500, are summarized in Table 4.1.

As can be seen from the table, all temperatures and humidity values lie within the operating ranges recommended by Agilent. In particular, the stable temperature in the STM laboratory has a positive effect on the reproducibility of the measurements and can be excluded as a major source of error during spring and summer. Future measurements

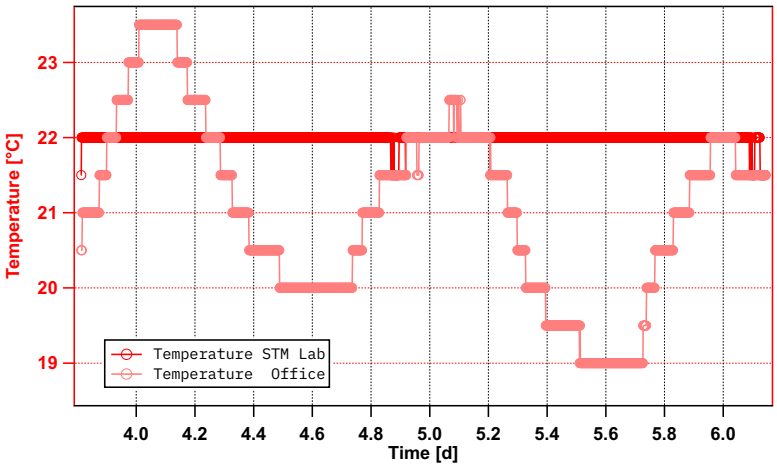

Figure 4.11: This graph shows an excerpt from Fig. 4.10, illustrating the temperature in the office and in the laboratory between day 4 and day 6. The day–night cycle is reflected in the temperature variations.

	min.	max.	Δ	$\langle x \rangle$
humidity				
office	29.5 %	59.0 %	29.5±0.5 %	45.0±6.9 %
STM laboratory	30.5 %	56.5 %	26.0±0.5 %	42.3±5.6 %
recommended by Agilent	15 %	95 %		
temperature				
office	18.5 °C	23.5 °C	5.0±0.5 °C	20.7±1.0 °C
STM laboratory	21.5 °C	22.5 °C	1.0±0.5 °C	21.9±0.2 °C
recommended by Agilent	5 °C	40 °C		

Table 4.1: Environmental parameters of temperature and humidity measured over 18 days in the laboratory, compared to the neighboring office. Shown are the minimum (min.) and maximum (max.) detected values for temperature (red) and humidity (blue), the difference between the global maxima (Δ), and the average values over 18 days with standard deviation ($\langle x \rangle$).

should also be performed during the winter months, since temperature fluctuations between the building interior and the outside environment are higher than in summer, and dry heating air has a strong influence on humidity.

Results 5

This chapter discusses the experiments conducted in the course of this master's thesis. The discussion begins with the determination of suitable potential limits for the subsequent electrochemical experiments, followed by the acquisition of STM images using the SPM 5500 and the documentation of aging processes of the sample observed during the measurements. Finally, two comparative approaches are presented: first, reference measurements are discussed to contextualize the potential response of the EC-experiments regarding the SPM 5500, and second, complementary AFM measurements are evaluated to characterize the thin-film surface morphology.

All data related to the SPM 5500 experiments were acquired using the built-in software PicoView 1.20. Data analysis, including calculations and data visualization, was performed using IGOR Pro 9, while Gwyddion was used for the processing and visualization of STM images.

5.1 Finding the right potential window

The EC-STM experiments performed in this work are based on studies reported by Yoshida *et al.*[8] and Wandlowski *et al.*[9]. In these publications, electrochemical investigations of gold thin films were carried out within potential windows ranging from −0.25 V up to 1.7 V, typically using 0.1 mol L^{-1} H_2SO_4 as the supporting electrolyte and a gold surface as working electrode. As the samples investigated in the present work had not been subjected to electrochemical measurements prior to this study, the following sections discuss the selection of suitable potential limits for the SPM 5500 system and the reasoning behind these choices in order to enable subsequent experiments.

For the electrochemical experiments, the prepared sample was mounted to an specimen disc and set magnetically into place on the sample holder (see figure 3.8). Prior to the measurements, the reference electrode was polarized at 6 V for 5 s in a beaker containing the 0.1 mol L^{-1} H_2SO_4 electrolyte solution (see Section 3.4) in order to load it with hydrogen and thus generate a Pt–H reference electrode. The electrode was subsequently reinserted into its holder using metal tweezers insulated with Teflon® tape.

After assembly of the solid components of the electrochemical cell, a droplet of the 0.1 mol L^{-1} H_2SO_4 solution is added to the surface of the WE. The Pt-H reference electrode (RE) was immersed as well as the Pt CE. Connecting the conductive silver paint by electrolyte was avoided. Due to the surface tension of the electrolyte, particular care had to be taken to ensure proper immersion of the electrodes within the droplet. Pre-wetting the electrodes with a small amount of electrolyte prior to assembly was found to facilitate the assembly of the experimental setup. The electrolyte volume was not defined, because the important part is the contact area between electrolyte and WE. [1] Prior to the measurements,

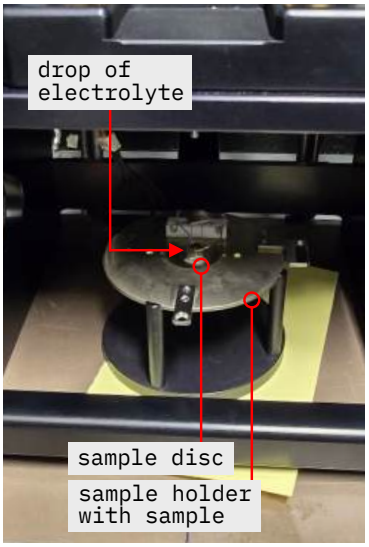

Figure 5.1: Photograph of the sample holder under the SPM 5500 scanning probe microscope, only attached to the internal potentiostat. The shown configuration represents the fundamental setup used for the EC measurement resulting in fig. 5.2.

1: In future experiments, the electrolyte volume could be determined more accurately by weighing or by dispensing a defined volume using an Eppendorf pipette, if required.

the 0.1 M H_2SO_4 electrolyte was purged with N_2 to eliminate dissolved oxygen. Approximately four times the flask volume was exchanged with nitrogen, in accordance with the commonly recommended three- to five-fold volume exchange for continuous N_2 purging. Notably, del Barrio-Galán *et al.* demonstrated that effective oxygen removal can be achieved even at lower purge volumes in wine.[26] However, the experiment was conducted under ambient conditions, making oxygen exchange with the electrolyte likely.

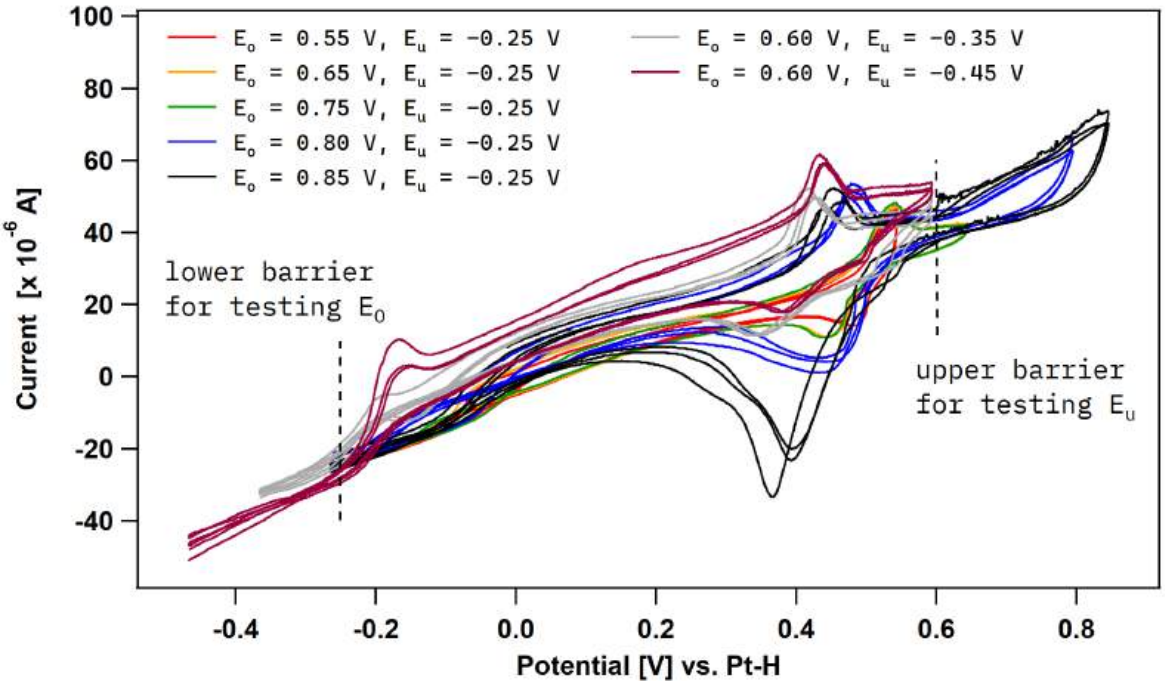

Figure 5.2: Overview of all recorded cyclic voltammograms (CVs) acquired at a constant scan rate of 20 mV s^{-1}. The current response is plotted as a function of the applied potential, measured versus the Pt-H RE. The measurement series is divided into two experimental sections with a constant lower reversal potential of $E_u = -0.25$ V and a constant upper reversal potential of $E_o = 0.6$ V, respectively.

The seven measurements are color-coded, and the corresponding parameters, including the lower (E_u) and upper (E_o) reversal potentials, are indicated accordingly. The first series (red, yellow, green, blue, and black) represents the parameter set used to identify the upper reversal potential, the second series (gray and wine-red) corresponds to the parameter set used to determine the lower reversal potential.

Due to the significantly different and more complex experimental setups employed in the studies of Yoshida *et al.*[8] and Wandlowski *et al.*[9], as well as the use of different reference electrode scales, a direct quantitative comparison was not pursued. Instead, a considerably narrower initial potential window was selected for the present work, depending on the results described below.

Based on these considerations, an initial potential window between $E_u = -0.25$ V and $E_o = 0.55$ V was selected. All measurements were carried out at a scan rate of 0.02 V s^{-1}. In total, seven different potential windows were investigated in order to identify the range in which the sample remains electrochemically stable for subsequent measurements. Each measurement consisted of three consecutive cycles (compare fig. 5.2).

The upper reversal potential was stepwise increased from 0.55 V (red)

to 0.65 V (yellow), 0.75 V (green), and 0.80 V (blue), respectively, while keeping the lower reversal potential constant. Upon a further increase by 0.05 V to E_o = 0.85 V (black), a new current response emerged in the potential range between 0.55 V and 0.6 V, which had not been observed in any of the previous measurements (compare fig. 5.3). In this final measurement a sudden increase in current of approximately 0.5×10^{-6} A was observed in the third cycle starting at around 0.6 V. Towards the upper reversal potential, the signal exhibited a pronounced noisy structure, which disappeared again at approximately 0.58 V during the reverse scan.

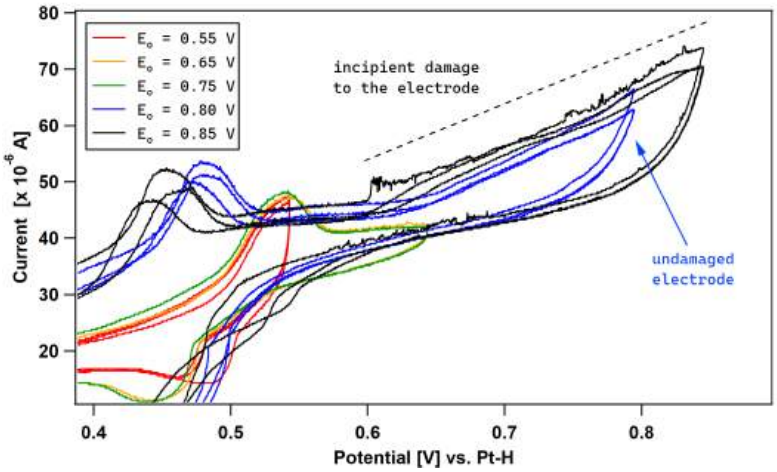

Figure 5.3: Representative cyclic voltammograms illustrating the onset of possably irreversible electrochemical behavior at extended potential limits.

Control measurements using a narrowed potential window with an upper reversal potential of 0.55 V remained fully reproducible even after the occurrence of these effects, indicating that no minor irreversible changes had occurred within this narrower potential range.

To determine the lower reversal potential E_u, the upper reversal potential was kept constant at 0.6 V, while the lower potential limit was stepwise decreased to −0.35 V (gray) and −0.45 V (wine red). For lower limits beyond −0.55 V, the CVs exhibited pronounced deviations in their cyclic characteristics compared to all previous measurements, as shown in figure 5.4.

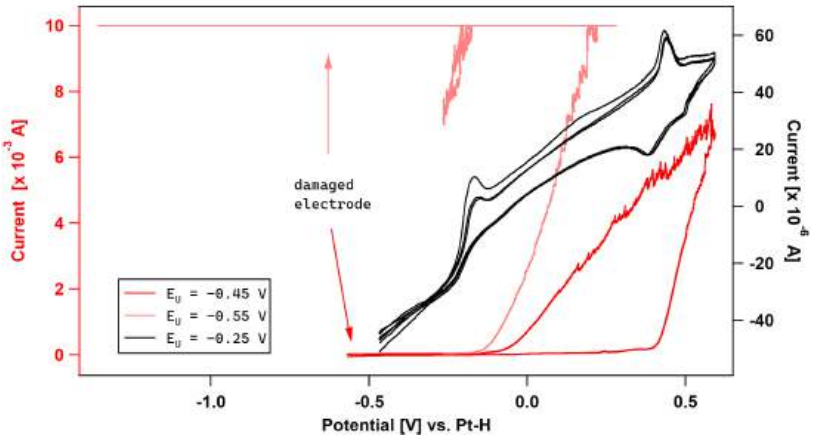

Figure 5.4: Cyclic voltammograms recorded at extended negative potentials. Note the change in the current scale of the y-axis.

As shown in Figure 5.4, the internal potentiostat integrated into the Agilent SPM 5500 reached its detection limits during this measurement (up to 10×10^{-3} A, differing by approximately three orders of magnitude

compared to the previous measurement). Consequently, the lower potential limit of −0.55 V could no longer be reliably accessed. To avoid possible damage to the instrument, the measurement was terminated after two cycles, and the sample was removed from the experimental setup.

After rinsing off the electrolyte, the sample exhibited pronounced optical changes. Gas bubble formation was observed, and the surface showed clear signs of corrosion. Below the position of the counter electrode—which was slightly bent away from the WE for improved visibility—the gold film had locally dissolved from the working electrode, thereby excavate the titanium adhesion layer. As a result of the applied negative potential, various titanium oxide layers formed, exhibiting their characteristic iridescent coloration.

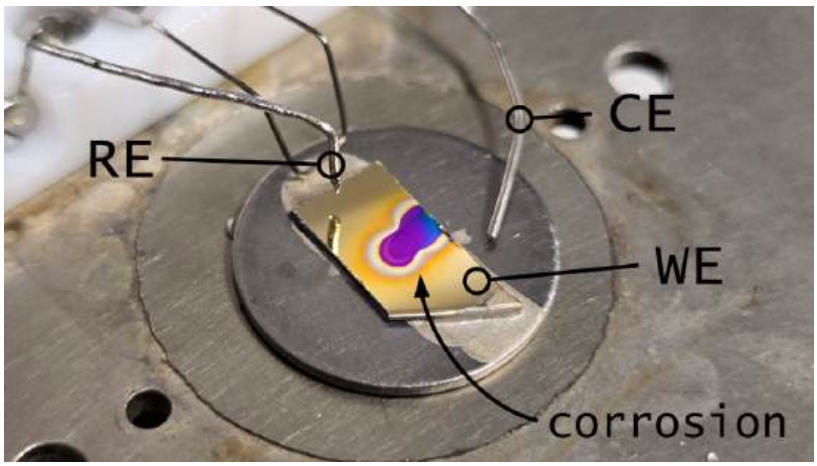

Figure 5.5: Photograph of the gold thin-film sample after rinsing with deionized water and drying, showing localized damage and corrosion-induced surface changes.

Based on these observations, a stable and reproducible potential window between $E_u = -0.25\,\mathrm{V}$ and $E_o = 0.55\,\mathrm{V}$ was identified and selected for all subsequent electrochemical and EC-STM measurements. The entire experiment lasted less than one hour.

This is relevant, as evaporation of water molecules become significant during longer measurements due to the small electrolyte volume, leading to a slight increase in electrolyte concentration over time, as further discussed in section 6.

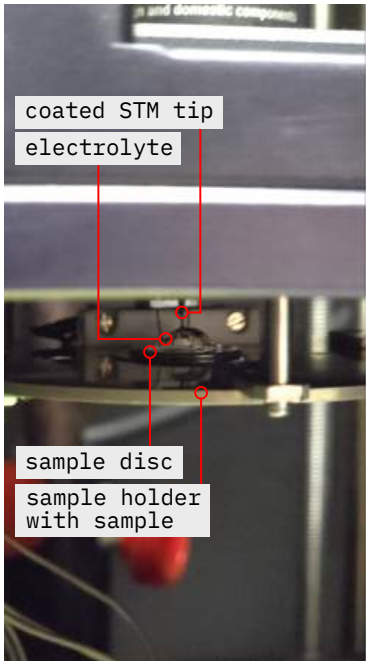

Figure 5.6: Photograph of the sample holder equipped with the STM tip as installed in the SPM 5500 scanning probe microscope. The shown configuration represents the fundamental setup used for EC-STM measurements.

5.2 EC-STM measurements

Electrode and thin-film preparation for the EC-STM experiments followed the procedure described in Section 5.1, using the same sample. Unlike in the first experiment, the sample holder was mounted inside the microscope, and the STM tip (type: KEYSIGHT N9802A-FG, see Section 3.1) was positioned close to the surface without electrical contact before being immersed in the electrolyte droplet (fig. 5.6). The climate chamber remained closed throughout the measurements to maintain constant atmospheric conditions.
The tunneling current setpoint was fixed at 0.5 nA, while the proportional and integral feedback gains were adjusted to 7 % and 70 %. All STM images were acquired using identical tunneling parameters. The sample bias voltage was set to 0.1 V for all measurements.

The lateral position of the scan area was not actively changed during the course of the measurements. Consequently, all STM images were acquired under nominally identical positioning conditions. However, due to unavoidable thermal drift, it cannot be excluded that slightly different surface regions were probed during the experiment. This interpretation is supported by subtle variations observed in the recorded STM images following in this section.

The EC-STM experiment was designed to investigate potential-induced structural rearrangements of the gold thin-film surface.

Figure 5.7 provides an overview of all eight cyclic voltammograms (CVs) recorded during the experiment, together with the corresponding STM imaging times and potential positions. The STM measurements were performed sequentially at electrode potentials of −0.2 V, 0.00 V, and 0.24 V within the anodic (oxidation) regime, followed by 0.1 V, 0.0 V, −0.14 V, and −0.2 V within the cathodic (reduction) regime. These potentials were selected because they are close to the ranges identified by Yoshida *et al.*[8] and most of them reside in stable areas, even with potential shifts, detected in the first experiment finding the potential window. Finally, an additional STM image was recorded again at 0.0 V in the anodic regime again to enable a direct comparison with the initial measurement at the same potential. At the end of this chapter the discussed STM images are collected in an overview (see Figure 5.17).
Prior to each STM acquisition, two complete CV cycles were recorded to allow the surface to rearrange and reorder. Subsequently, the potential was driven to the target value and held for approximately 5 s to permit partial stabilization of the electrochemical interface, after which the STM image was acquired.

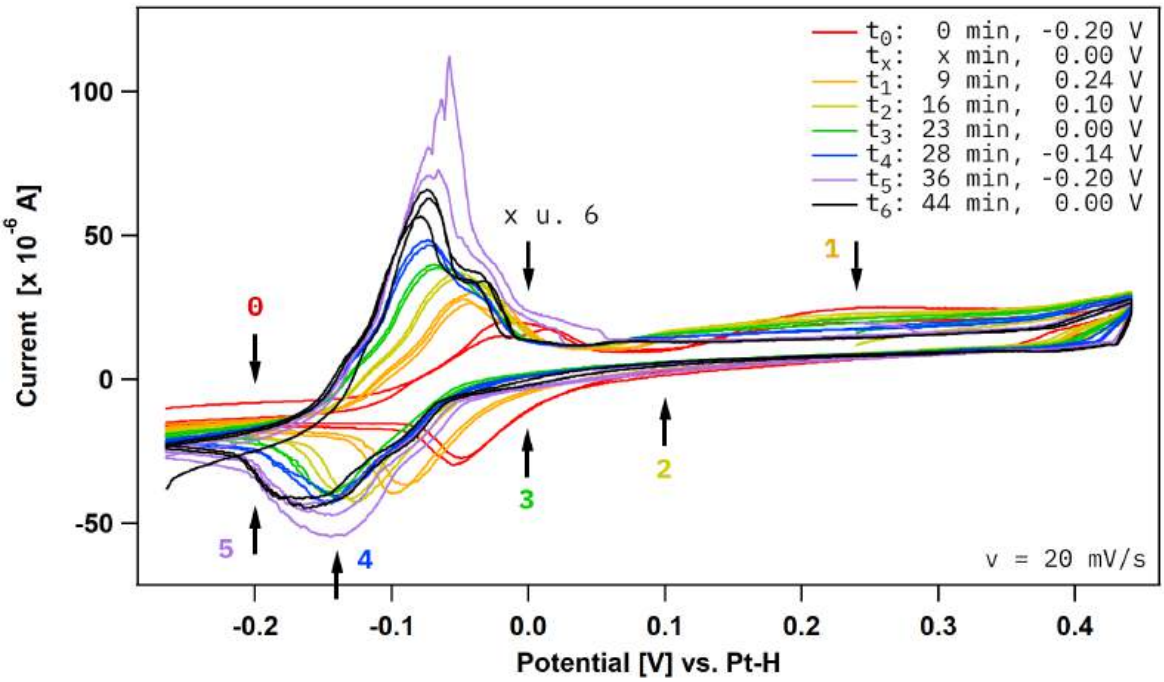

Figure 5.7: Overview of all recorded cyclic voltammograms (CVs) corresponding to the eight STM images discussed below, with marked positions and time stamps. The current density is plotted as a function of the electrode potential measured versus a Pt–H reference electrode in 0.1 mol L^{-1} H_2SO_4.

Due to a faulty data storage process, the electrochemical data of mea-

surement t_x were lost. This measurement was performed within a time window between 2 and 7 min; however, the corresponding STM data are available. The entire experiment lasted approximately 46 min. For each CV, two measurement cycles were recorded, and all CVs were acquired at a scan rate of 20 mV s^{-1}.

The following five pages present the color-coded STM images corresponding to markers 0, x, and 1 to 6 in Figure 5.7.

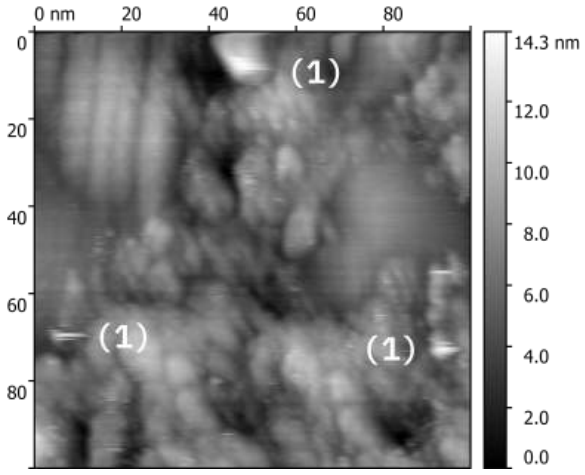

(a) STM topographic image (trace) acquired at open-circuit potential (OCP). The image was recorded with a resolution of 256 × 256 pixels over an area of 100 nm × 100 nm. The line speed was set to 15 lines s^{-1}. The scan direction was upward.

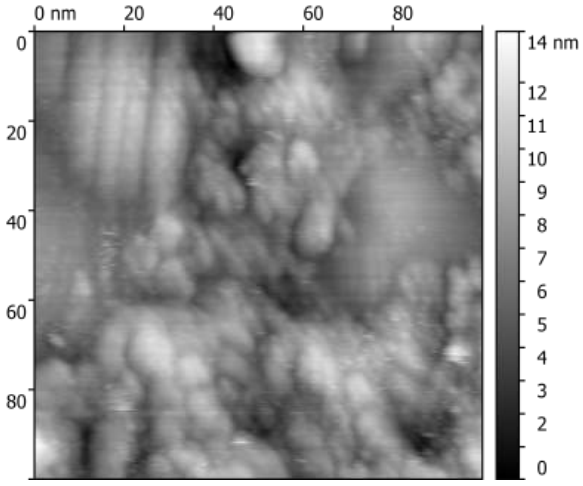

(b) STM topographic image (retrace) acquired at open-circuit potential (OCP). The image was recorded with a resolution of 256 × 256 pixels over an area of 100 nm × 100 nm. The line speed was set to 15 lines s^{-1}. The scan direction was upward.

Figure 5.8: STM images recorded at open-circuit potential prior to electrochemical polarization. No potential was initialized in this measurement, but it is conducted in the electrolyte.

Cloud-like structures are observed in Figure 5.8, exhibiting height variations of up to 14 nm. Owing to the relatively slow scan rate of 15.15 lines s^{-1}, horizontal line artifacts are visible across both images (a) and (b). The prominent white features in (a), marked as (1), indicate the presence of (organic) contaminants on the sample surface indicated by a flag-like feature to the right. Both the trace (a) and retrace (b) images display very similar characteristics, suggesting that the measurement was performed under stable conditions.

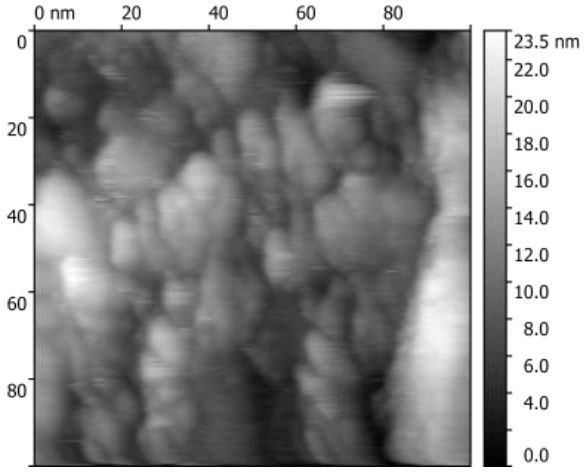

(a) STM topographic image (trace) acquired at an electrode potential of −0.2 V. The image was recorded with a resolution of 256 × 256 pixels over an area of 100 nm × 100 nm. The line speed was set to 15 lines s^{-1}. The scan direction was upward.

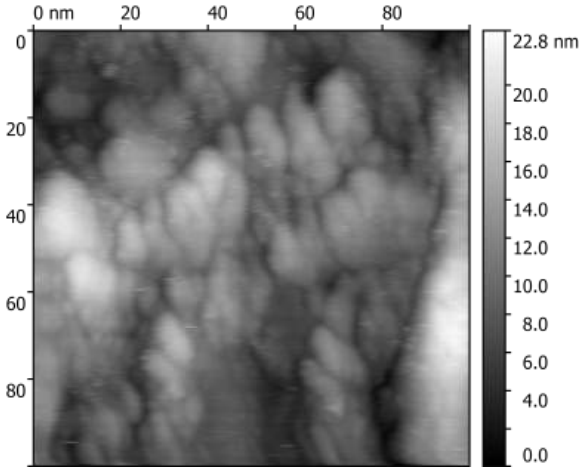

(b) STM topographic image (retrace) acquired at an electrode potential of −0.2 V. The image was recorded with a resolution of 256 × 256 pixels over an area of 100 nm × 100 nm. The line speed was set to 15 lines s^{-1}. The scan direction was upward.

Figure 5.9: STM images acquired at the position inicated by `marker 0 - t0: -0.2 V` during the anodic (oxidation) sequence.

The surface imaged in Figure 5.9 differs markedly in its morphology from that observed surface in the previous images (Figure 5.8). Scale-like features have formed, exhibiting height variations of up to 23.8 nm. Minor measurement artifacts, which may originate from surface contamination or electronic noise, appear as small fragments approximately 5 nm in length and one scan line in width. The overall data quality is high, as the trace and retrace images are nearly identical. At the lower edge of image (a), slight indications of hysteresis are observed within a height range of approximately 0 to 5 nm, whereas no such behavior is

evident in image (b).

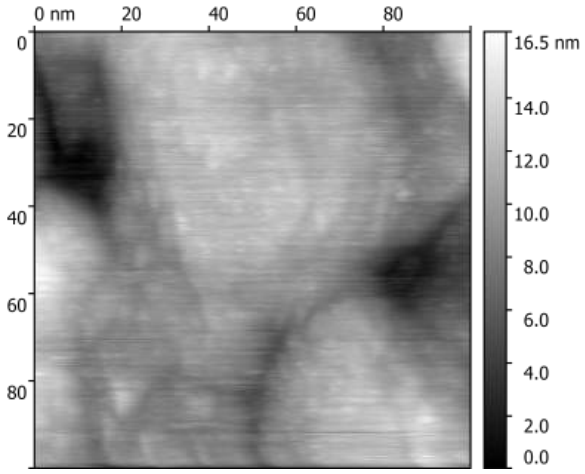

(a) STM topographic image (trace) acquired at an electrode potential of 0 V. The image was recorded with a resolution of 256 × 256 pixels over an area of 100 nm × 100 nm. The line speed was set to 15 lines s^{-1}. The scan direction was upward.

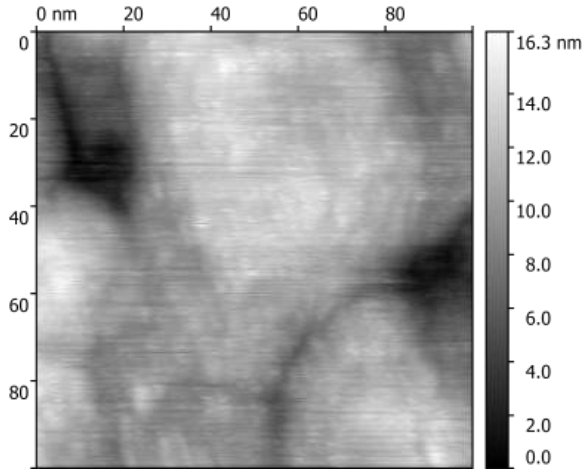

(b) STM topographic image (retrace) acquired at an electrode potential of 0 V. The image was recorded with a resolution of 256 × 256 pixels over an area of 100 nm × 100 nm. The line speed was set to 15 lines s^{-1}. The scan direction was upward.

Figure 5.10: STM images acquired at the position inicated by `marker x - t6 0 V` during the anodic (oxidation) sequence.

In Figure 5.10 the previously scale-like structures have transformed into nearly uniform plateaus, exhibiting height variations of up to 16.3 nm. Horizontal artifacts in the fast scan direction (x-direction) increase noticeably across the entire image, while the previously observed smaller artifacts have almost completely disappeared. The surface has evolved into a new terrace-like morphology. Trace (a) and retrace (b) images again show excellent agreement, indicating stable measurement conditions.

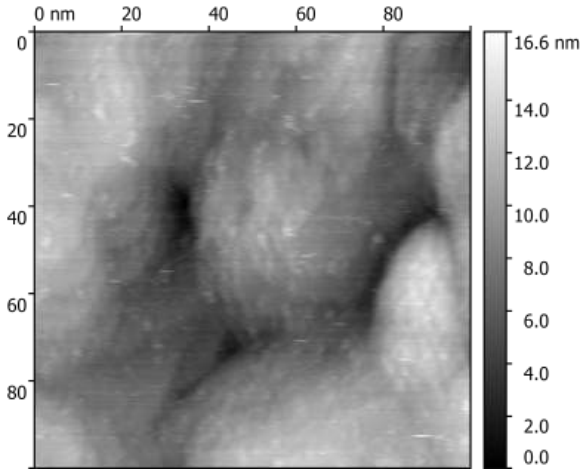

(a) STM topographic image (trace) acquired at an electrode potential of 0.24 V. The image was recorded with a resolution of 256 × 256 pixels over an area of 100 nm × 100 nm. The line speed was set to 15 lines s^{-1}. The scan direction was upward.

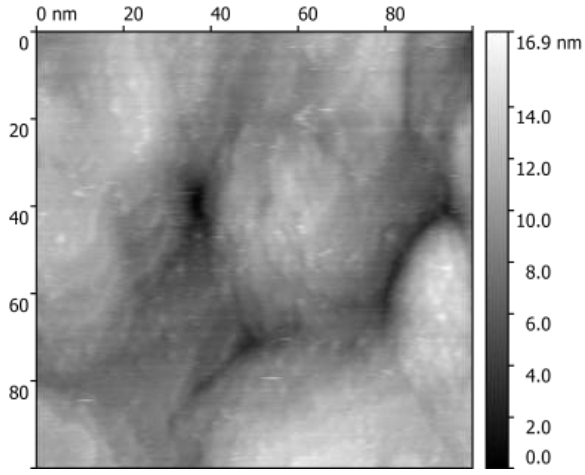

(b) STM topographic image (retrace) acquired at an electrode potential of 0.24 V. The image was recorded with a resolution of 256 × 256 pixels over an area of 100 nm × 100 nm. The line speed was set to 15 lines s^{-1}. The scan direction was upward.

Figure 5.11: STM images acquired at the position inicated by `marker 1 - t1: 0.24 V` during the anodic (oxidation) sequence.

In Figure 5.11 surface morphology changes from terrace-like to more rounded features. Horizontal artifacts persist, and the 5 nm disturbances previously observed reappear. Two lower-lying features appear closer to each other; however, this observation cannot be unambiguously confirmed due to two cleaning EC cycles performed prior to imaging. Trace (a) and retrace (b) images again show excellent agreement, indicating stable measurement conditions.

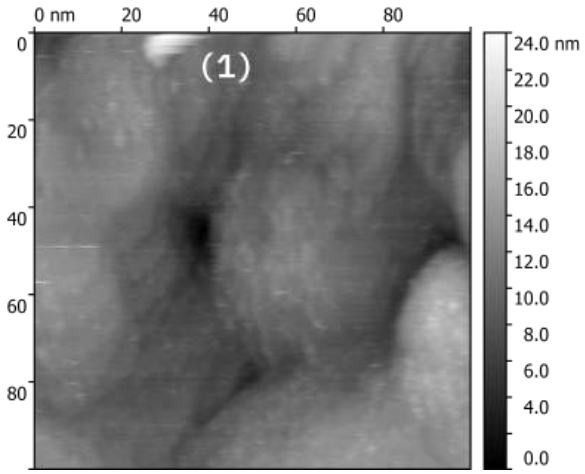

(a) STM topographic image (trace) acquired at an electrode potential of 0.1 V. The image was recorded with a resolution of 256×256 pixels over an area of 100 nm × 100 nm. The line speed was set to 15 lines s^{-1}. The scan direction was upward.

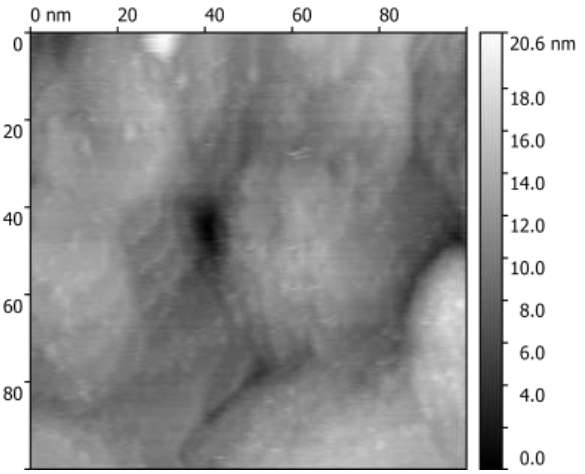

(b) STM topographic image (retrace) acquired at an electrode potential of 0.1 V. The image was recorded with a resolution of 256 × 256 pixels over an area of 100 nm × 100 nm. The line speed was set to 15 lines s^{-1}. The scan direction was upward.

Figure 5.12: STM images acquired at the position inicated by `marker 2 - t2: 0.1 V` during the cathodic (reduction) sequence.

Very similar surface features are observed in this Figure 5.12 compared to Figure 5.11. Although height variations of up to 24 nm are detected (1), these elevations are attributed to possible surface contamination. When such contributions are excluded, the present image is nearly identical to the preceding one, showing structures with height variations of about 16 nm. Trace (a) and retrace (b) images again show excellent agreement, indicating stable measurement conditions.

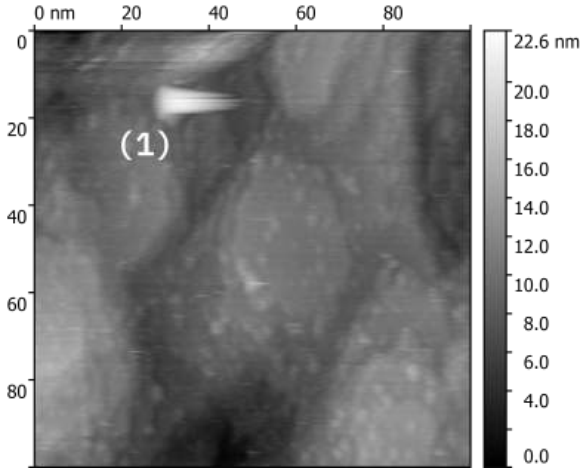

(a) STM topographic image (trace) acquired at an electrode potential of 0 V. The image was recorded with a resolution of 256 × 256 pixels over an area of 100 nm × 100 nm. The line speed was set to 15 lines s^{-1}. The scan direction was upward.

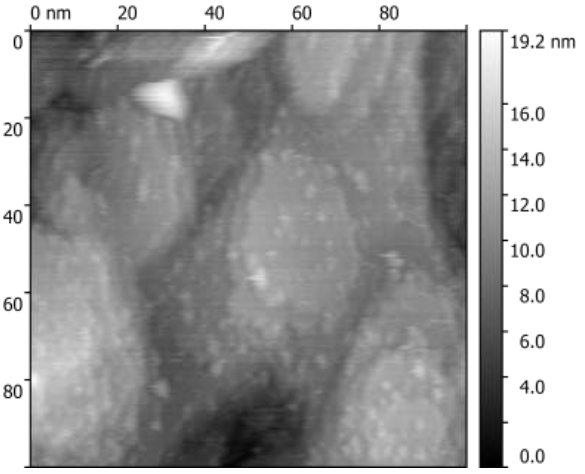

(b) STM topographic image (retrace) acquired at an electrode potential of 0 V. The image was recorded with a resolution of 256 × 256 pixels over an area of 100 nm × 100 nm. The line speed was set to 15 lines s^{-1}. The scan direction was upward.

Figure 5.13: STM images acquired at the position inicated by `marker 3 - t3: 0 V` during the cathodic (reduction) sequence.

Considering the bright feature (1) in Figure 5.13a, a thermally induced shift of approximately 1.4 nm during the measurement is estimated, corresponding to about 10 nm over 7 min based on the time stamps in Figure 5.7. The surface reorganizes toward terrace-like structures, with height variations of approximately 16 nm when the contribution of feature (1) is excluded. Trace (a) and retrace (b) images again show excellent agreement, indicating stable measurement conditions.

The image pair presented in Figure 5.14 is the only one exhibiting distinct differences between the trace (a)

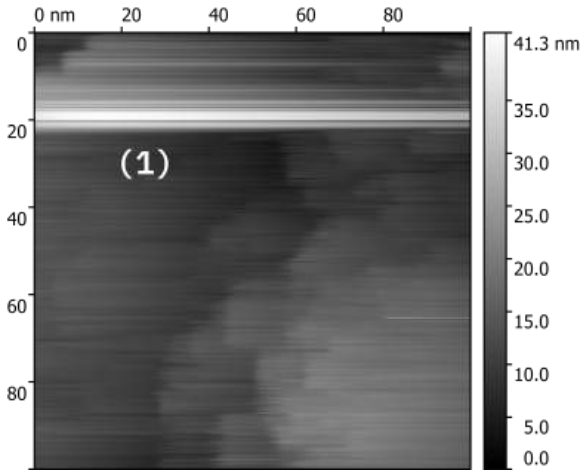

(a) STM topographic image (trace) acquired at an electrode potential of −0.14 V. The image was recorded with a resolution of 256 × 256 pixels over an area of 100 nm × 100 nm. The line speed was set to 15 lines s^{-1}. The scan direction was upward.

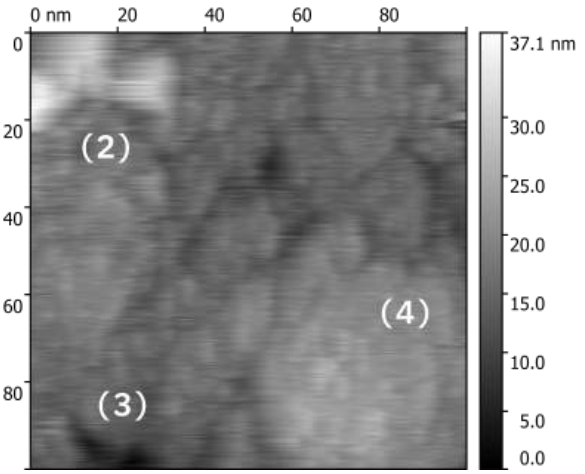

(b) STM topographic image (retrace) acquired at an electrode potential of −0.14 V. The image was recorded with a resolution of 256 × 256 pixels over an area of 100 nm × 100 nm. The line speed was set to 15 lines s^{-1}. The scan direction was upward.

Figure 5.14: STM images acquired at the position inicated by `marker 4 - t4: -0.14 V` during the cathodic (reduction) sequence. The newly formed surface morphology observed in image (b) again exhibits a scale-like structure. When feature (2) is excluded and the height difference between regions (3) and (4) is considered, characteristic height variations of approximately 20 nm are obtained.

and retrace (b). The elongated feature marked as (1) in image (a) suggests that contamination was dragged along the fast scan direction by the STM tip during the trace scan. No corresponding feature is observed in the retrace image. This image is included in the present analysis for transparency, as such elongated features can easily be mistaken for needle-like structures that may occur on gold surfaces. However, additional measurements in which the scan direction was varied confirmed that this feature does not rotate with the scan orientation, thereby identifying it as a measurement artifact rather than a genuine surface structure.

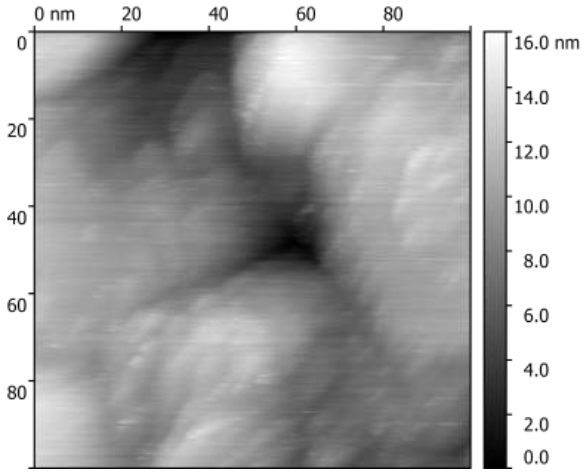

(a) STM topographic image (trace) acquired at an electrode potential of −0.2 V. The image was recorded with a resolution of 256 × 256 pixels over an area of 100 nm × 100 nm. The line speed was set to 15 lines s^{-1}. The scan direction was upward.

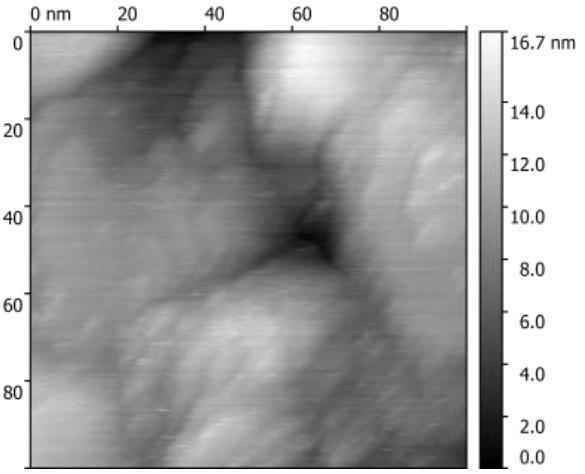

(b) STM topographic image (retrace) acquired at an electrode potential of −0.2 V. The image was recorded with a resolution of 256 × 256 pixels over an area of 100 nm × 100 nm. The line speed was set to 15 lines s^{-1}. The scan direction was upward.

Figure 5.15: STM images acquired at the position inicated by `marker 5 - t5: -0.2 V` during the cathodic (reduction) sequence. Trace (a) and retrace (b) images again show excellent agreement, indicating stable measurement conditions.

The measurement shown in Figure 5.15 was performed at the same potential as the images shown in Figure 5.9; however, the resulting surface morphology differs markedly. Terrace-like structures are again observed, exhibiting height variations of up to 16.7 nm. The same measurement artifacts as those identified in

Figure 5.13 are present, whereas no scale-like features can be discerned.

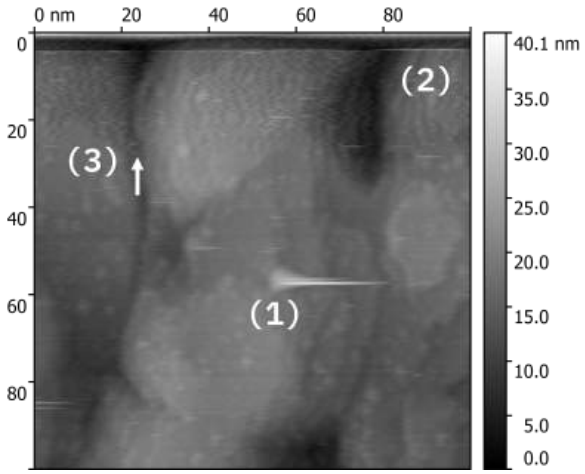

(a) STM topographic image (trace) acquired at an electrode potential of 0 V. The image was recorded with a resolution of 256 × 256 pixels over an area of 100 nm × 100 nm. The line speed was set to 15 lines s^{-1}. The scan direction was upward.

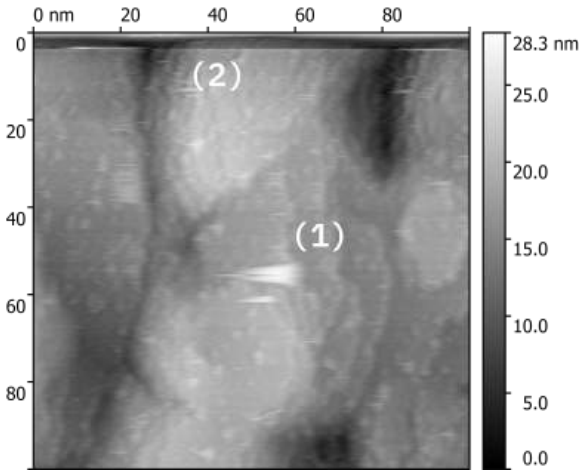

(b) STM topographic image (retrace) acquired at an electrode potential of 0 V. The image was recorded with a resolution of 256 × 256 pixels over an area of 100 nm × 100 nm. The line speed was set to 15 lines s^{-1}. The scan direction was upward.

Figure 5.16: STM images acquired at the position inicated by `marker 6 - t6 0 V` in the final step to assess reproducibility and to compare with the second measurement (see fig. 5.10) at the same potential in the oxidation cycle.

This measurement, presented in Figure 5.16, exhibits effects similar to those observed in the previously recorded images shown in Figure 5.10. Terrace-like structures are again apparent, exhibiting height variations of approximately 20 nm when the bright feature marked as (1), which is likely associated with surface contamination, is excluded. The surface morphology shown here is not identical to that observed in Figure 5.10. At the upper edge of both the trace (a) and retrace (b) images, a measurement artifact marked as (2) is present, which locally reduces the apparent height variations from approximately 20 nm to about 10 nm. The origin of this effect remains unclear, and further measurements could not be performed with this sample. In the trace image (a), features characteristic of electronic noise become apparent above a y-coordinate of approximately 25 nm to 0 nm, as indicated by (3). Apart from these height-related artifacts, the trace (a) and retrace (b) images show excellent agreement, indicating stable measurement conditions.

The STM images clearly demonstrate a pronounced influence of the applied electrode potential on the surface structure of the gold thin film. For most measurements, trace and retrace images are qualitatively consistent, indicating stable tunneling conditions. A notable exception is observed at −0.14 V (fig. 5.14), where localized differences are attributed to transient contamination. This effect does not persist in subsequent measurements.

Overall, the EC-STM results confirm potential-induced surface restructuring and demonstrate the sensitivity of the technique for correlating electrochemical behavior with nanoscale surface morphology.

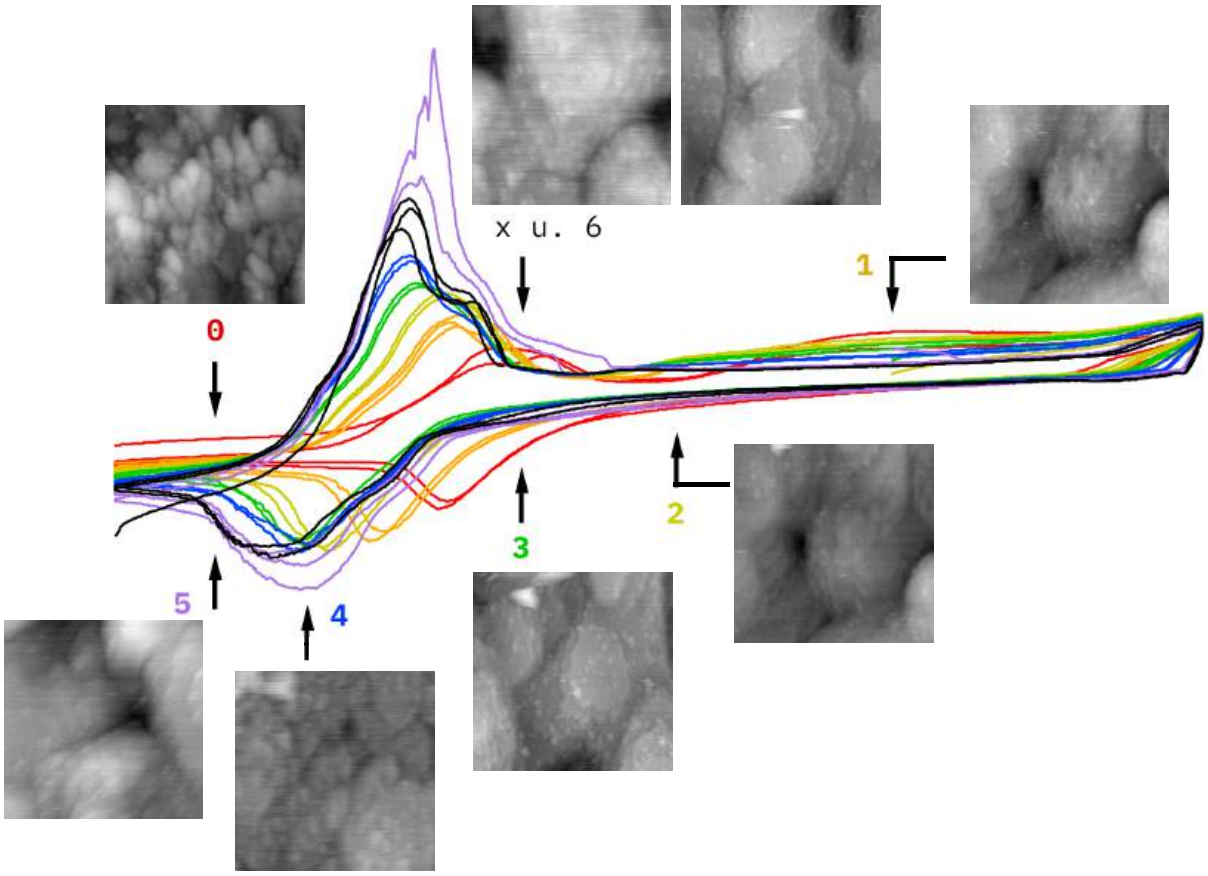

Figure 5.17: Combined representation of electrochemical and structural data. The cyclic voltammograms shown correspond to the dataset presented in Fig. 5.7 and are displayed using identical axis scaling. The numbered markers indicate the electrode potentials at which the STM measurements were performed. For each marked position, the corresponding STM image is shown, displaying the surface morphology of the gold thin film over an area of 100 nm × 100 nm at the respective electrochemical state. The STM images were selected from the corresponding trace/retrace pairs based on the lowest number of visible scanning artefacts in order to ensure optimal image quality.

The overview shown in Figure 5.17 enables a direct comparison between the potential-dependent surface structures observed by EC-STM and the corresponding electrochemical response. It further provides a basis for comparison with literature data, in particular with the results reported by Yoshida *et al.* and Wandlowski *et al.*[8, 9], as discussed section 6.

5.3 Aging processes during EC measurements

During the course of the EC-STM experiments (see section 5.2), pronounced changes in the electrochemical response were observed not only upon exchanging samples, but also during prolonged measurements performed on the same sample. In order to systematically quantify these effects, the positions of characteristic current peaks and their corresponding electrode potentials were extracted as a function of time and evaluated for all subsequent experiments. The aim of this analysis was to assess the temporal stability of the electrochemical system, with particular focus on potential drift effects related to the Pt-H reference electrode and possible aging phenomena of the gold thin-film electrode.

All potentials reported in this chapter are referenced to a Pt-H reference electrode. Due to the geometry of the experimental setup, the use of alternative reference electrodes, such as Ag/AgCl, was not feasible, as commercially available standard electrodes were too large to be accommodated.

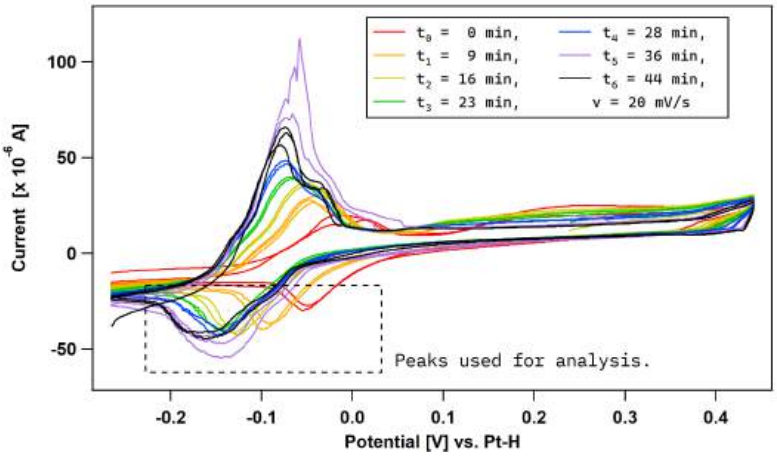

Figure 5.18: Cyclic voltammogram with highlighted peak regions used for the electrochemical analysis of peak current density and the associated peak potential shift.

For the EC-STM measurements, the temporal evolution of the peak potential and peak current density was evaluated. The peak positions were determined semi-automatically using a cursor-based approach. For each data point, the values were averaged over the corresponding measurement cycle (two cycles per measurement). As the experiment was not conducted continuously, the starting time of each cycle was used as the reference point for the time axis (see fig. 5.19).

Symbol	Description	Unit
A	Amplitude of y_0	V
y_0	Final value / offset	V
τ	Time constant	min

Table 5.1: Parameters used for the exponential fit.

The data reveal a systematic shift of the characteristic peak potentials towards more negative values over time. At this stage, a definitive assignment of this potential drift is not possible, as only a single EC-STM measurement series is available. A likely contribution may arise from gradual hydrogen desorption from the Pt-H reference electrode, leading to a slow change in its effective reference potential.

In contrast to the EC-STM measurements described above, an additional

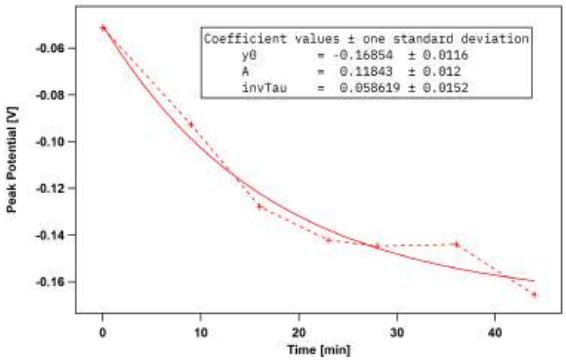

(a) Temporal evolution of the peak potential extracted from the EC-STM measurements. The potential values represent averages over the respective measurement cycles and are plotted as a function of time in minutes.

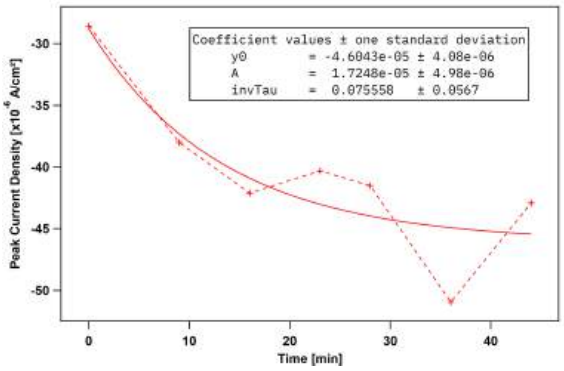

(b) Temporal evolution of the peak current density extracted from the EC-STM measurements. The values represent averaged peak current densities plotted as a function of time in minutes.

Figure 5.19: Temporal evolution of peak potential (a) and corresponding peak current density (b) extracted from the EC-STM measurements. Both quantities were obtained from identical peak regions and averaged over the respective cycles, allowing direct correlation of potential drift and current response during STM operation. The solid line represents a power fit of the form $y(x) = y_0 + A \exp\left(-\frac{x}{\tau}\right)$ (see table 5.1). The fit parameters are shown in the boxes. The data are listed in Tables **??** and 6.1 at the end of this chapter.

long-term electrochemical stability experiment was performed in EC-only mode using the same sample and the same SPM 5500 system on the following day. In this experiment, no STM imaging was carried out. Instead, a continuous cyclic voltammetry measurement was conducted over a total duration of 30 min at a scan rate of 20 mV s^{-1}. The upper reversal potential was reduced to $E_o = 0.3$ V, as previous experiments had shown that oxidation at higher potentials can strongly modify the surface structure of the gold thin film. The lower reversal potential was kept constant at $E_u = -0.25$ V.

Each cycle had a duration of approximately 1.2 min (72 s) and consisted of 8014 data points, reflecting the technical limitations of the internal potentiostat of the SPM 5500. Over the full measurement time, a total of 25 cycles were recorded (see fig. 5.20).

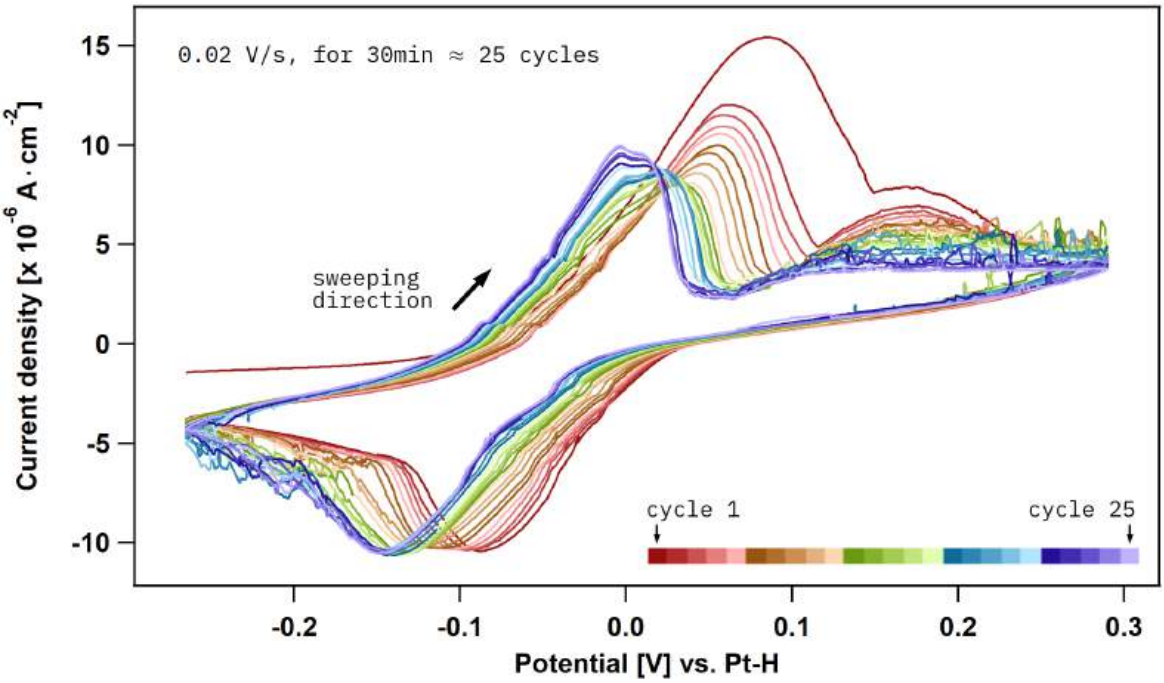

Figure 5.20: Continuous cyclic voltammetry measurement over 30 min recorded at a scan rate of 20 mV s^{-1}. Individual cycles are color-coded for clarity.

With increasing cycle number, enhanced fluctuations in the current density were observed near the potential limits of the voltammograms. This behavior emerged from approximately the fifth cycle (corresponding to about 4 min) and persisted until the end of the experiment at cycle 25. Such increasing fluctuations may indicate progressive structural degradation or corrosion of the thin film. They could also be associated with increased surface mobility of gold atoms, leading to potential-induced surface restructuring, which is consistent with the trends observed in the STM measurements (see Figure 5.17).

If these fluctuations were solely attributable to electrical noise, the observed effects would not be confined to specific potential regions. Instead, a similar behavior is observed in both the oxidation half-cycle and, starting from a potential of approximately −0.15 V, in the reduction half-cycle. As the limits of the applied potential window are approached, it can be assumed that adsorbed hydrogen species may gradually participate in H_2 formation. In these potential regions, pronounced changes in surface structure are also observed, as evidenced by the STM data (cf. Figure 5.17).

The transferred charge during oxidation and reduction was determined by integrating the current density over time. From this, the number of transferred electrons can be calculated according to $n = Q/e$, where Q is the integrated charge and e is the elementary charge (e.g. 5.22)

For the evaluation, the oxidation peak labeled A was compared with the subsequent reduction peak A′. The immediately following peak after A was excluded from the analysis, as its current response became increasingly fluctuend over time and did not yield reproducible results. The peak separation between A and A′ was approximately 0.14 V. The evaluated values for the charge density are shown in Figure 5.24.

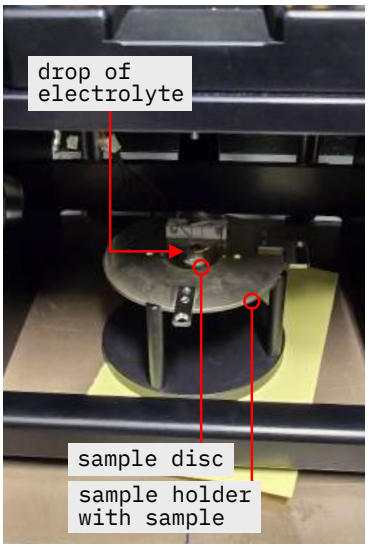

Figure 5.21: Photograph of the sample holder under the SPM 5500 scanning probe microscope, only attached to the internal potentiostat. The shown configuration represents the fundamental setup used for the "long time" EC measurement shown in fig. 5.20.

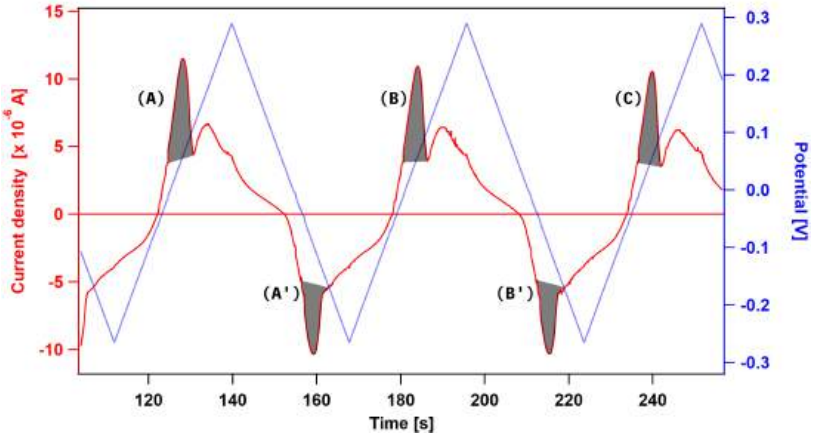

Figure 5.22: Excerpt from the current density and potential versus time representation derived from Fig. 5.20. The red curve shows the current response of the cyclic voltammogram, while the blue curve indicates the applied electrode potential. The shaded gray areas mark the peak regions that were integrated and compared to determine the transferred charge.

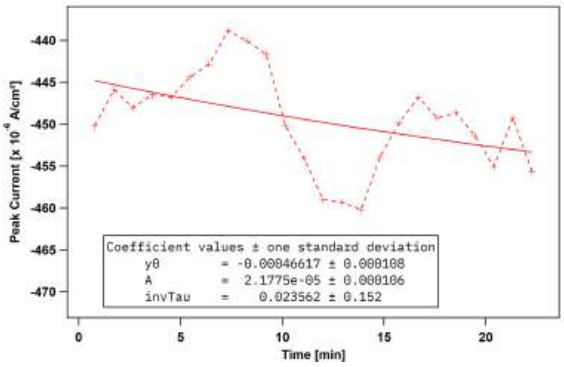

(a) Peak current density as a function of time for the long-term EC-only measurement.

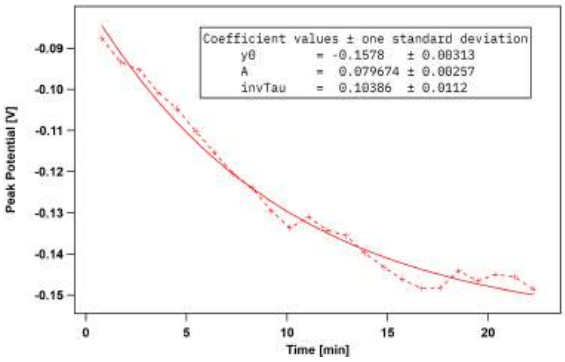

(b) Temporal evolution of the peak potential for the long-term EC-only measurement.

Figure 5.23: Temporal evolution of peak current density (left) and corresponding peak potential (right) during the long-term EC-only measurement. Both quantities were extracted from identical peak regions and averaged over the respective cycles. The data are listed in Table and 6.1 at the end of this chapter.

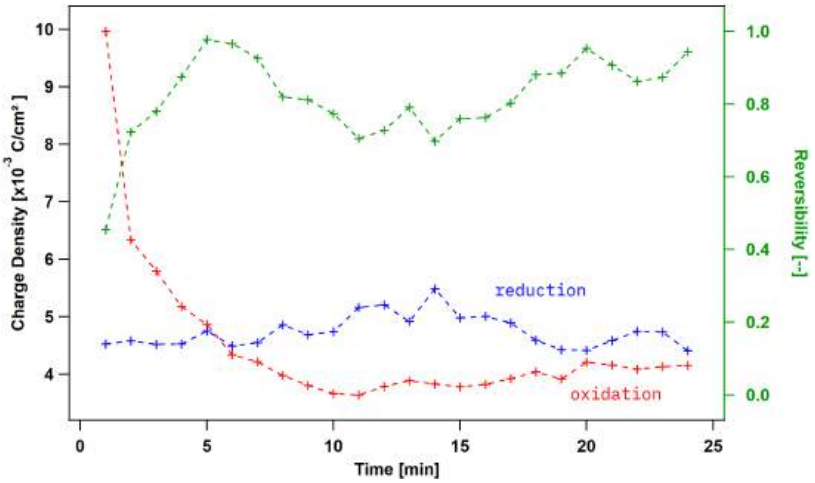

Figure 5.24: In this graph, the transferred charge densities (normalized to the electrode area) are plotted as a function of time. From the ratio of the oxidation charge density (red) to the reduction charge density (blue), the reversibility was calculated in order to assess the electrochemical behavior of the system.

At the beginning of the measurement, a pronounced change in the transferred charge density by approximately a factor of 2.5 is observed. After about 10 min, the charge density (oxidation) appears to stabilize. The reversibility, calculated from the ratio of the oxidation and reduction charge densities, tends toward a nearly constant value between 1 and 0.8; however, the available data set is too limited to allow for a more quantitative assessment.

The temporal evolution of the transferred charge was modeled using the exponential decay function of the form $y(x) = y_0 + A \exp\left(-\frac{x}{\tau}\right)$ where τ denotes a characteristic decay time with the same unit as the time axis. This functional form was chosen as a phenomenological model, as a first-order process may be involved, for example related to gradual hydrogen desorption from the Pt-H reference electrode or slow interfacial rearrangements. A definitive mechanistic assignment, however, cannot be made based on the present data and is therefore not pursued further.

After completion of the long-term experiment, the sample was rinsed with Milli-Q water and dried upside down in a magnetic holder to minimize dust contamination. A reproduction of the electrochemical response using identical experimental parameters, electrolyte, and instrumentation on the following day was not successful (see fig. 5.25).

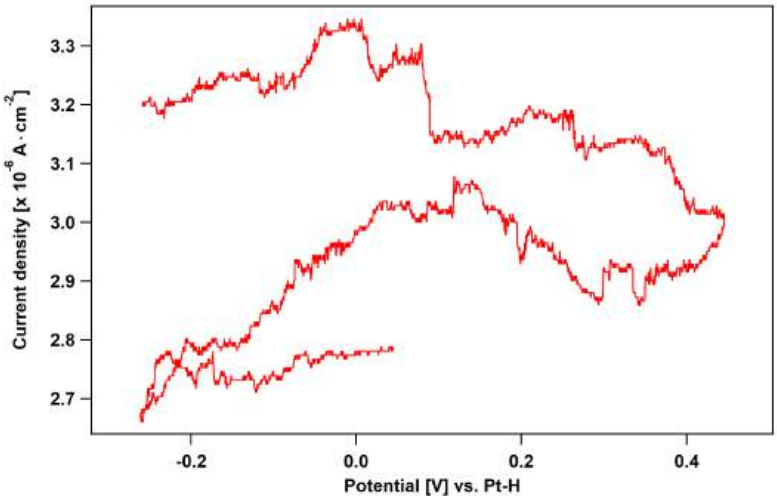

Figure 5.25: Attempt to reproduce the cyclic voltammogram obtained prior to the long-term measurement. The current density is plotted as a function of the electrode potential versus the Pt-H reference electrode.

The reproduced cyclic voltammogram shows pronounced deviations compared to the original measurement. While current densities and potential ranges remain within the same order of magnitude, the signal exhibits clear digital artefacts and unstable regulation of the internal potentiostat, characterized by oscillations between discrete current levels and incomplete cycle closure. Despite variations of measurement parameters and repeated attempts, no qualitatively improved data could be obtained using the same sample. Consequently, further measurements with this setup were discontinued, motivating the subsequent experiments performed using the external AGEF potentiostat.

5.4 Comparison measurements using the AGEF potentiostat

Due to the inconsistent and partially irreproducible electrochemical results obtained with the internal potentiostat of the SPM 5500, comparative measurements were performed using a well-established external potentiostat. For this purpose, the AGEF potentiostat described in Chapter 3.1 was employed. This system is routinely used in the advanced laboratory courses in chemistry and has been validated over many years through numerous electrochemical studies conducted under the supervision of

Dr. Detlef Diesing. In addition, the instrument is regularly maintained and calibrated by the in-house electronics technician Werner Saure.

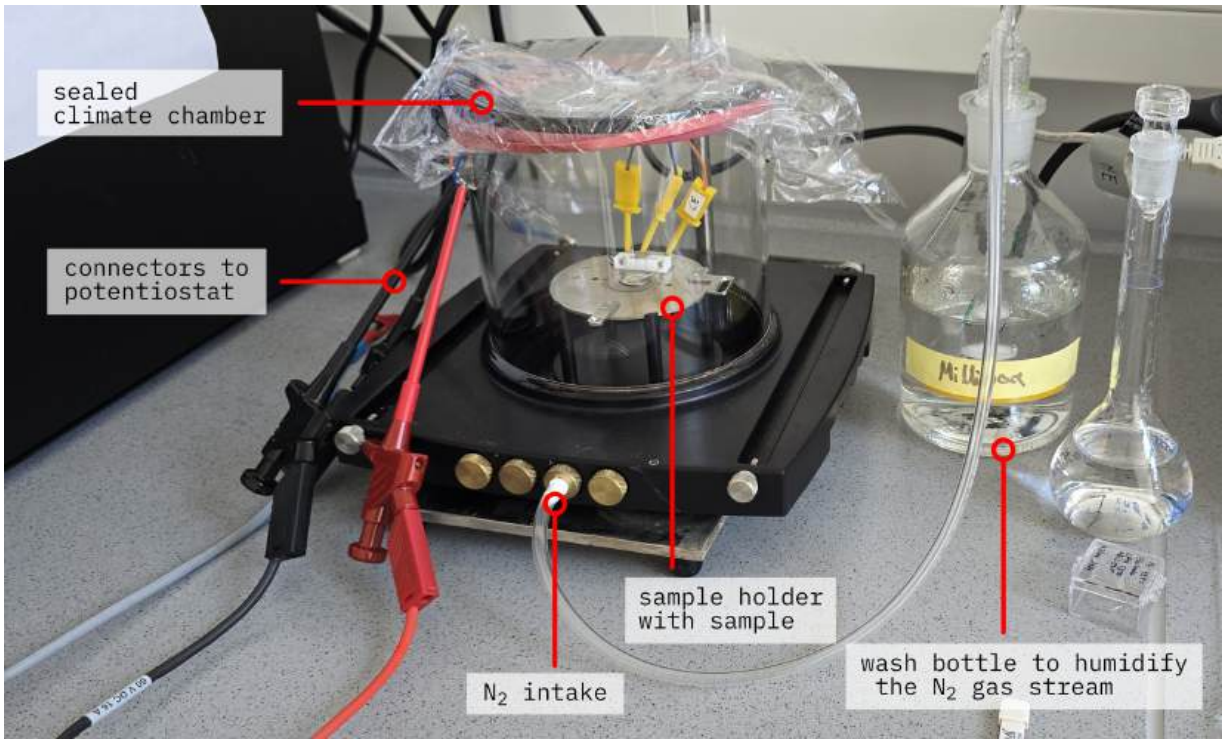

Figure 5.26: Photograph of the experimental setup used for the electrochemical measurements with the AGEF potentiostat. The sample holder containing the gold thin-film electrode was placed inside the climate chamber originally used for the SPM 5500 measurements. Electrical contact to the potentiostat was established using small crocodile clips. The chamber was sealed using plastic film and rubber bands, with a small opening allowing excess gas to escape. The same sample as used for the EC-STM measurements was employed.

In contrast to the EC-STM setup, STM imaging is not possible in the AGEF configuration. However, the electrochemical cell geometry and electrode materials were kept identical to those used in the SPM 5500 experiments in order to ensure maximum comparability. The gold thin film served as the working electrode, a Pt-H-loaded platinum wire was used as the reference electrode, and a platinum counter electrode was employed. All potentials reported in this chapter are given with respect to the Pt-H reference electrode.

As evaporation of the electrolyte droplet was identified as a limiting factor in the EC-STM experiments, the AGEF measurements were performed under a humidified nitrogen atmosphere. A continuous stream of N_2 gas saturated with Milli-Q water was applied to maintain a stable electrolyte volume and to ensure oxygen-free conditions. The electrochemical cell was placed inside the climate chamber originally associated with the SPM 5500, which remained closed throughout the measurements and was kept under a slight nitrogen overpressure.

To achieve a stable and homogeneous gas flow, a wash bottle equipped with a fine porous frit was used to generate a large number of small gas bubbles, thereby ensuring efficient humidification of the nitrogen stream.

Data acquisition was carried out using the software *MephistoScope1*. The recorded CSV files were subsequently processed and analyzed using IGOR Pro 9.

After reevaluating the potential window, six cyclic voltammograms (CVs) were recorded at different scan rates of 20, 50, 100, and two measurements at 150 mV s^{-1}, (see fig. 5.27).

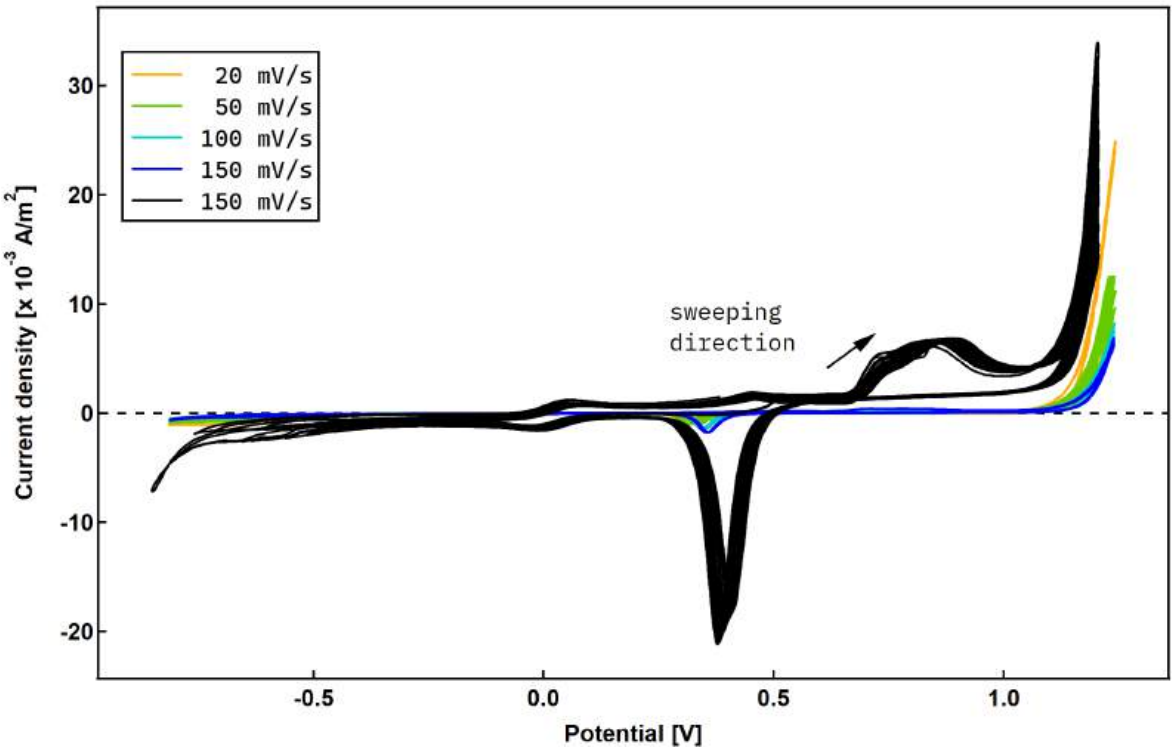

Figure 5.27: Overview of cyclic voltammograms recorded with the AGEF potentiostat at scan rates of 20, 50, 100, and 150 mV s^{-1}. The current density is plotted as a function of the applied electrode potential versus the Pt-H reference electrode. The data shown represent raw, unprocessed measurements.

Compared to the data acquired with the internal SPM 5500 potentiostat, the raw AGEF data exhibited a current noise level of approximately 100×10^{-6} A cm^{-2} (e.g. fig. 5.28). In order to improve comparability with the SPM-based measurements, the AGEF data were smoothed using a boxcar averaging algorithm with a smoothing factor of 200. This procedure represents a necessary post-processing step and does not qualitatively alter the electrochemical features of interest. Both raw and smoothed data are shown where appropriate.

The applied smoothing operation is described by

$$\overline{x}[i] = \frac{1}{2M+1} \sum_{j=-M}^{M} x[i+j],$$

which corresponds to a box-shaped averaging window of width $2M + 1$ (see WaveMetrics Website[2]). At high smoothing factors and for datasets with a limited number of points, this procedure can reduce sharp peak intensities, particularly near the reversal potentials. However, given the large number of data points in the present measurements, a smoothing factor of 200 was found to sufficiently reduce noise without significantly affecting peak positions or integrated charges.

2: WaveMetrics - Smoothing[27]

To illustrate the influence of the smoothing procedure applied to the AGEF data, Fig. 5.28 shows a representative section of the measurement

recorded at a scan rate of $5\,\mathrm{mV\,s^{-1}}$. The raw data (black) exhibit current fluctuations of approximately $100\times10^{-6}\,\mathrm{A\,cm^{-2}}$, whereas application of a smoothing factor of 200 reduces this noise level to about $10\times10^{-6}\,\mathrm{A\,cm^{-2}}$. The scan direction is indicated by the black arrow.

To directly compare the performance of the AGEF potentiostat with that of the SPM 5500 internal potentiostat, cyclic voltammograms recorded at a scan rate of $20\,\mathrm{mV\,s^{-1}}$ were overlaid (see fig. 5.29).

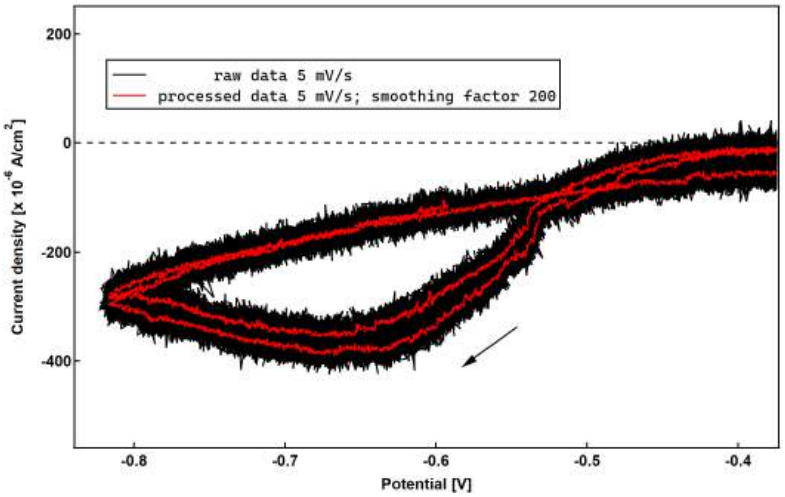

Figure 5.28: Comparison of raw (black) and smoothed (red) AGEF data for a measurement recorded at $5\,\mathrm{mV\,s^{-1}}$. The smoothing factor of 200 effectively reduces noise while preserving the electrochemical features relevant for further analysis.

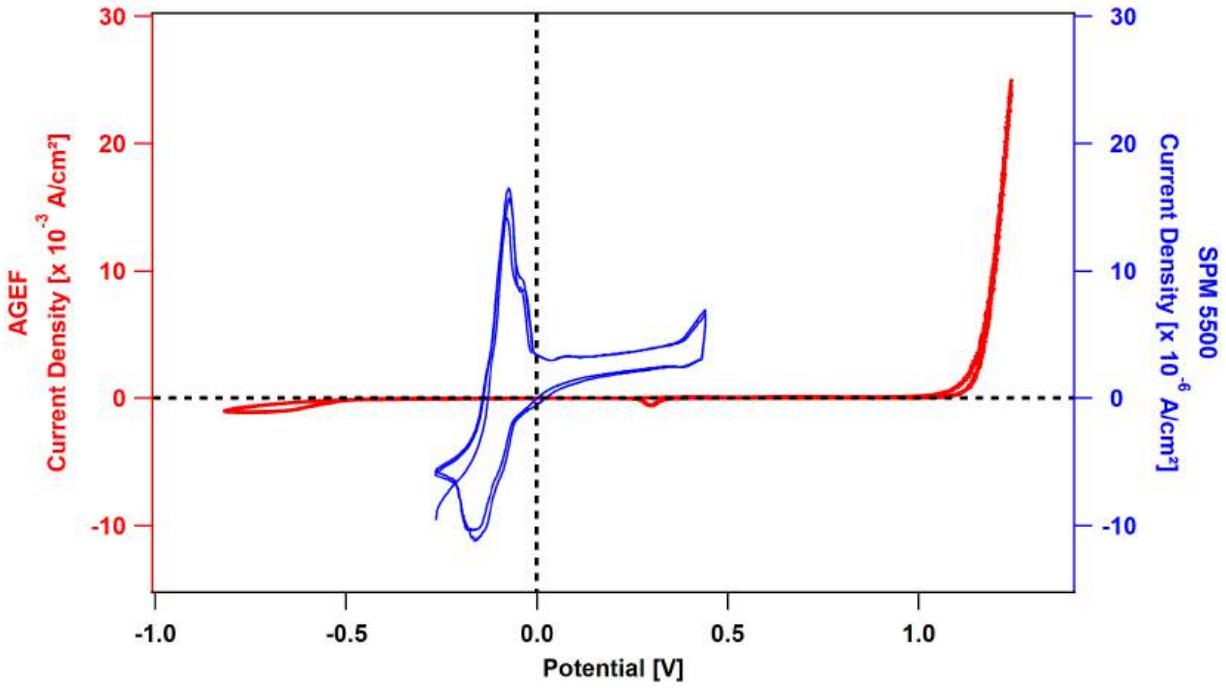

Figure 5.29: Comparison of cyclic voltammograms recorded at $20\,\mathrm{mV\,s^{-1}}$ using the SPM 5500 internal potentiostat (blue) and the AGEF potentiostat (red). Current densities are plotted as a function of electrode potential versus the Pt-H reference electrode.

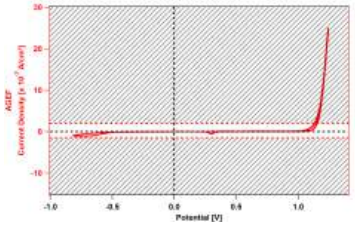

Figure 5.30: Highlighted potential region selected for the enlarged comparison shown in Fig. 5.31. While the potential limits remain unchanged, the current

The two datasets (AGEF - red, SPM - blue) show pronounced qualitative differences in curve shape, accessible potential window, and absolute current density. In particular, the AGEF potentiostat allows for significantly wider potential windows to be applied without observable signs of

corrosion in the recorded current responses. Furthermore, the measured current densities differ by up to three orders of magnitude between the two systems.

Personal Note

If the samples had not originated from the same wafer and if their preparation had not been performed personally under identical conditions, a direct correlation between the measurements obtained with the two potentiostats would appear highly unlikely.

To allow a more detailed comparison between the AGEF data and the SPM data, a section of the current density trace from Figure 5.30 was selected and replotted in Figure 5.31. Neither qualitative nor quantitative agreement between the two data sets can be identified.

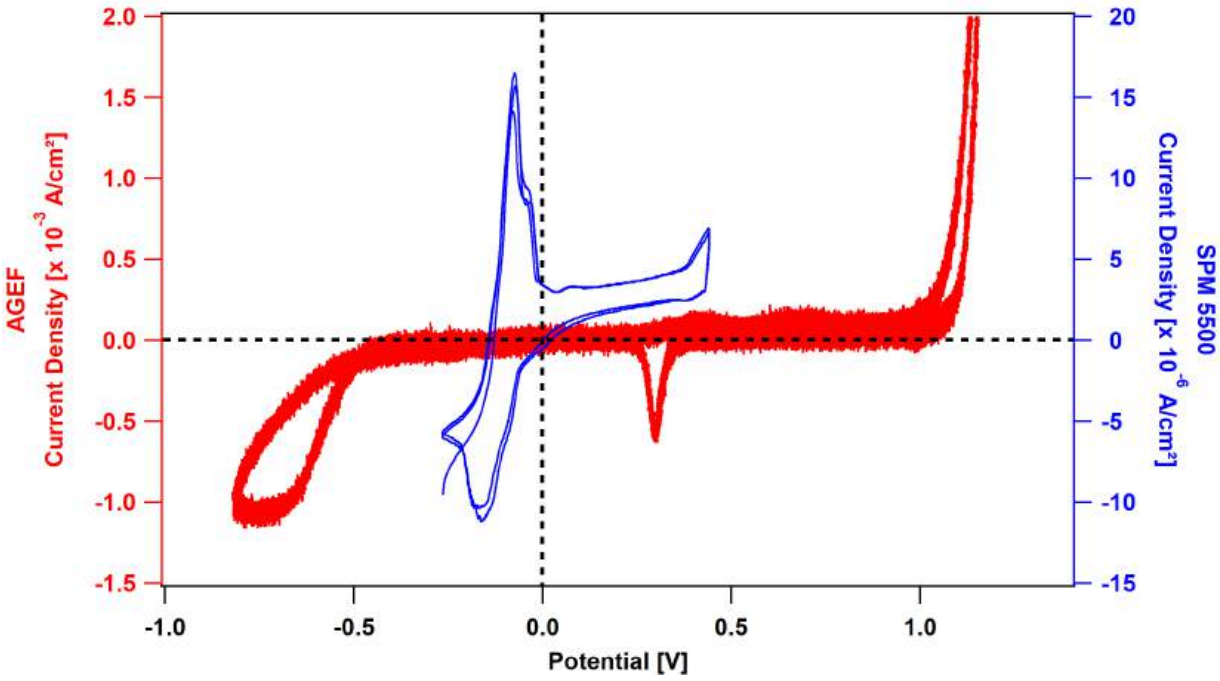

Figure 5.31: Enlarged comparison of cyclic voltammograms recorded at 20 mV s^{-1} using the SPM 5500 internal potentiostat (blue) and the AGEF potentiostat (red). The improved signal quality of the AGEF data allows for the resolution of additional electrochemical features, particularly in the reduction region.

A long-term stability experiment was performed at a scan rate of 150 mV s^{-1} after completion of all other AGEF measurements. This experiment was initiated 56 min after the beginning of the measurement series and was continued for a total duration of 23 min.

The position of the prominent reduction peak shown in Figure 5.32 was plotted, as before, as a function of peak current density versus time and peak potential versus time, as shown in Figure 5.33.

For the quantitative evaluation, the oxidation peak A was compared with the subsequent reduction peak A'.

The potential shift and current shift values are listed in Table 6.1.

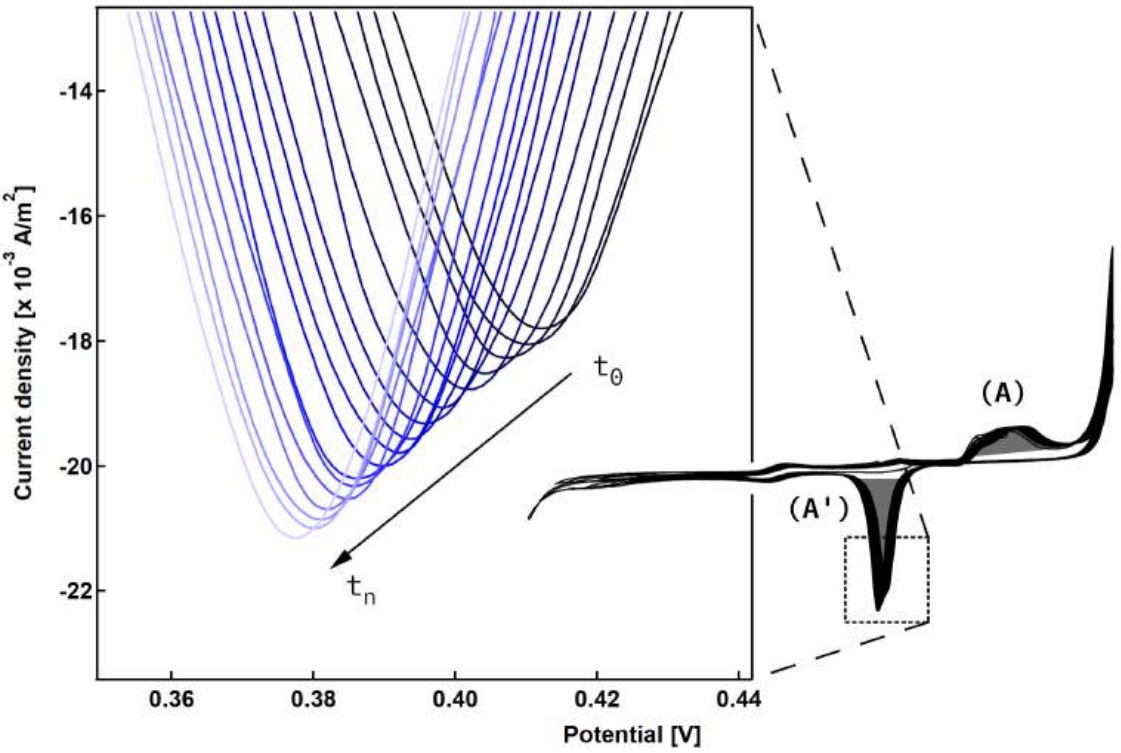

Figure 5.32: Time-resolved representation of the prominent reduction peak obtained during the long-term AGEF measurement at 150 mV s^{-1}. Individual cycles are color-coded from black (t_0) to light blue (t_n). The black curve shows the complete cyclic voltammogram with the selected peak regions for oxidation (A) and reduction (A′) highlighted in gray.

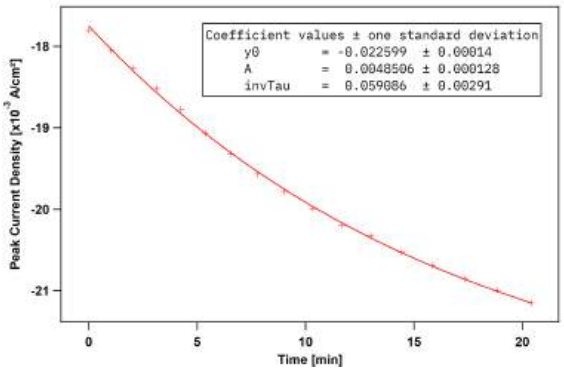

(a) Peak current density as a function of electrode potential extracted from the long-term AGEF measurement. Temporal information is not explicitly included.

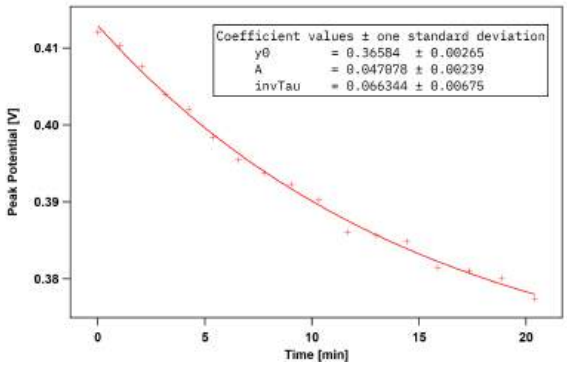

(b) Temporal evolution of the peak potential extracted from the long-term AGEF measurement. The values represent averages over the respective cycles.

Figure 5.33: Evolution of characteristic peak parameters extracted from the long-term AGEF measurement. The left panel shows the temporal shift of the peak potential, while the right panel correlates the corresponding peak current density with electrode potential. Both quantities were obtained from identical peak regions and averaged over the respective cycles.

The transferred charge was determined by integrating the current density over time and converting the resulting charge into the number of transferred electrons according to $n = Q/e$. The evolution of the oxidation and reduction charges and their corresponding reversibility are shown in Fig. 5.34.

Overall, the AGEF potentiostat provides significantly more stable and reproducible electrochemical data under the investigated conditions. The observed differences relative to the SPM 5500 measurements are

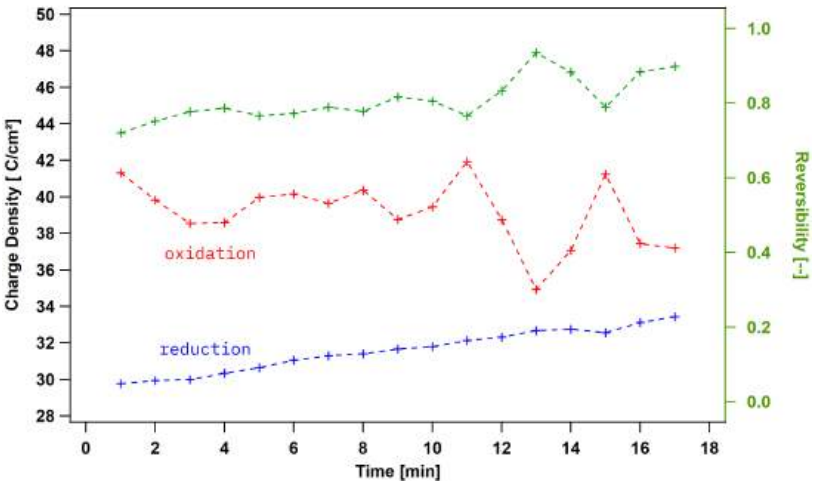

Figure 5.34: In this graph, the transferred charge densities (normalized to the electrode area) are plotted as a function of time. From the ratio of the oxidation charge density (red) to the reduction charge density (blue), the reversibility was calculated in order to assess the electrochemical behavior of the system.

attributed to instrumental limitations of the internal potentiostat when operated under EC-STM conditions.

5.5 AFM images

As no additional AFM or STM system was available within the working group, the samples were examined after the experiments using a Bruker AFM provided by ICAN[3]. The measurements were performed by Dr. Steffen Franzka, who was also involved in the fabrication process of the samples used in this work. For these measurements, the sample from the EC-STM measurements was analyzed.

The following images were acquired by Dr. Franzka and made available for this work. All images were recorded using a Bruker AFM[4] operated in tapping mode. The measurements were performed in ambient air at room temperature. Prior to the AFM measurements, the sample were rinsed with Millipore water.[5] The raw data is provided in the digital appendix.

It should be noted that AFM measurements do not provide time-resolved information on dynamic electrochemical processes. Instead, they yield a static characterization of the surface morphology and thus describe the structural initial conditions of the sample. These measurements therefore provide a structural reference for the interpretation of the electrochemical and EC-STM results discussed in the preceding chapters.

The AFM images reveal that the gold thin film does not form a closed and continuous layer. Instead, the surface is characterized by agglomerated structures that are present across the surface and exhibit typical heights in the range of approximately 12 to 15 nm.

This surface morphology indicates that the underlying titanium adhesion layer, which is located between the gold film and the silicon substrate, is locally exposed. As a consequence, the electrochemical system cannot be regarded as a purely gold-based electrode. Instead, a mixed system is present, in which electrochemical processes may occur at the gold surface, at exposed titanium regions, and at interfacial areas between both materials. Such a situation is expected to significantly affect the

3: Interdisciplinary Center for Analytics on the Nanoscale at the University Duisburg-Essen

4: *Bruker Dimension Icon:* Capable of topographic imaging with a lateral resolution smaller than 20 nm and a vertical resolution smaller than 0.1 nm, using a maximum scan area of 90 µm × 90 µm and a maximum z-range of 10 µm, with image resolutions of up to 5120 × 5120 pixels. – Advertisement flyer of ICAN[28].

5: An oxygen plasma treatment to remove possible organic contaminants was not applied, as it leads to oxidation of the gold layer and irreversible damage to the sample. - It was tested with a different sample.

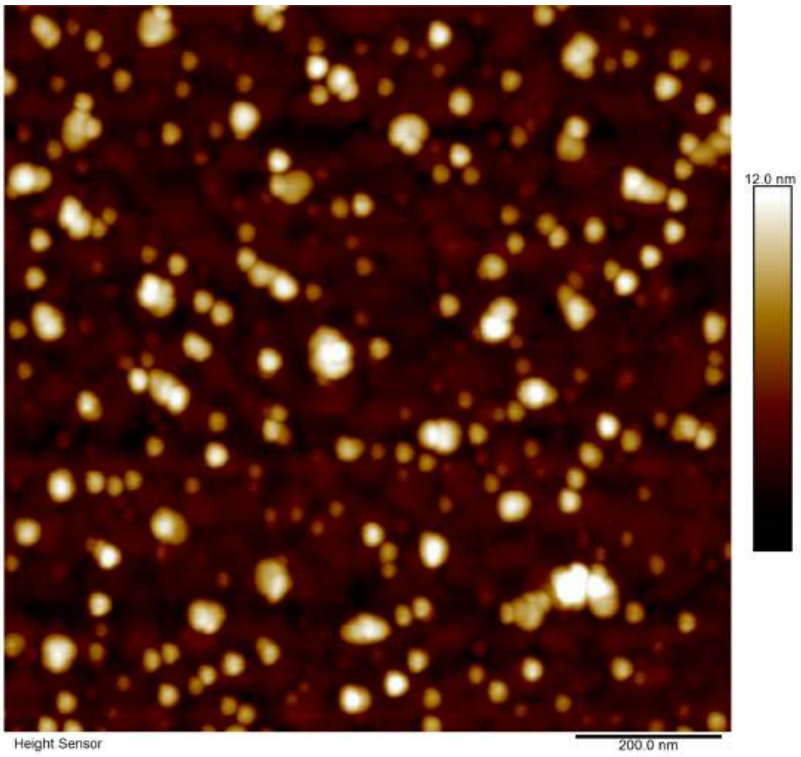

Figure 5.35: AFM topography of the sample surface acquired in tapping mode. The image shows the surface morphology over an area of 1000 nm × 1000 nm. Height differences between individual surface features of up to 12 nm are represented, ranging from dark (0 nm) to white (12 nm).

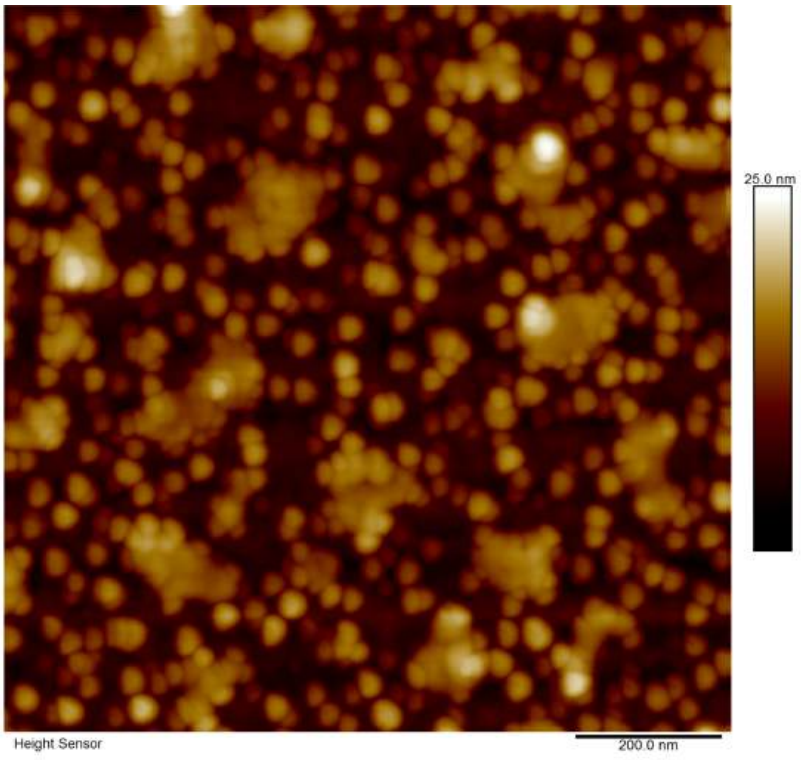

Figure 5.36: AFM topography of the sample surface acquired in tapping mode. The image shows the surface morphology over an area of 1000 nm × 1000 nm. Height differences between individual surface features of up to 25 nm are represented, ranging from dark (0 nm) to white (25 nm).

electrochemical response, as gold and titanium exhibit markedly different electrochemical properties in acidic media.

Furthermore, the observed surface structures are strongly inhomogeneous and vary depending on the lateral position on the sample. As a result, a reproducible electrochemical response across different measure-

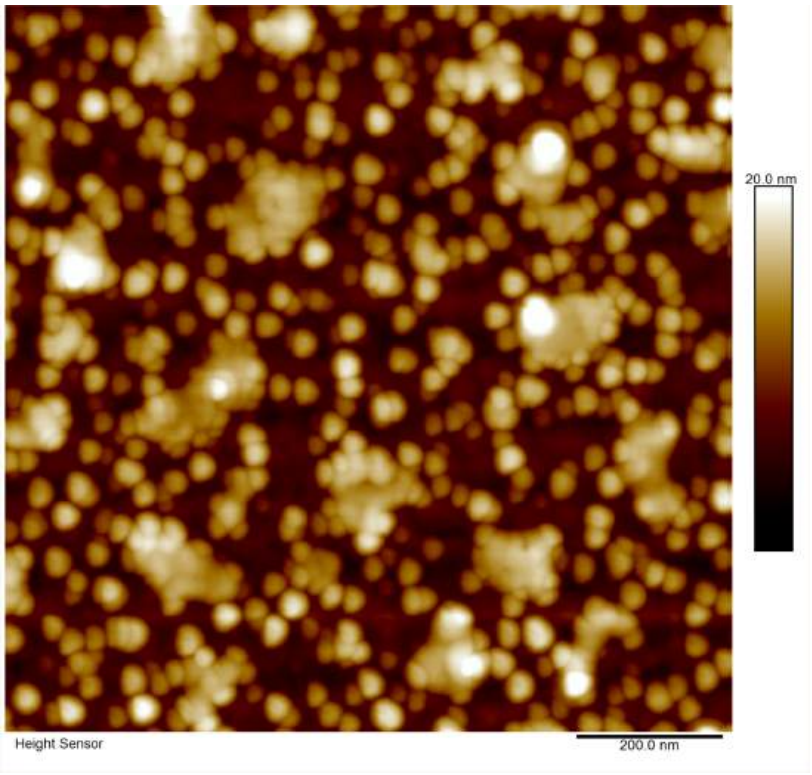

Figure 5.37: AFM topography of the sample surface acquired in tapping mode. The image shows the surface morphology over an area of 1000 nm × 1000 nm. Height differences between individual surface features of up to 20 nm are represented, ranging from dark (0 nm) to white (20 nm).

ment locations, including EC-STM measurements, cannot be expected. This provides a plausible structural explanation for the limited reproducibility observed in the electrochemical and EC-STM measurements discussed in the preceding chapters.

Discussion 6

This section discusses and integrates the results presented in Chapter 5. The discussion first focuses on the comparable features observed in the electrochemical (EC) measurements, followed by a comparison of the AFM and STM data.

6.1 EC-Data

In this section, the collected electrochemical (EC) data are evaluated, as summarized in Table 6.1.

Experiment	$\tau_{\text{peak potential}}$ [s]	$\tau_{\text{peak current density}}$ [s]
EC-STM	3.52 ± 0.91	4.53 ± 3.40
EC-SPM	6.23 ± 0.67	1.23 ± 8.40
AGEF	3.98 ± 0.41	3.55 ± 0.17

Table 6.1: Extracted time constants for the potential shift and current shift.

The data collected in the table are plotted in Figure 6.1.

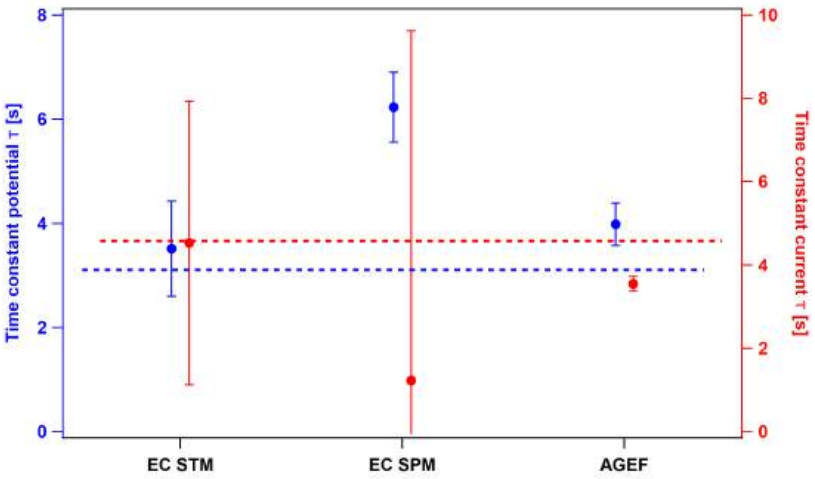

Figure 6.1: This graph shows the decay time constants for the potential shift (blue) and the current shift (red), plotted as a function of the experiments presented in Chapter 5. The dashed lines indicate the mean decay time constant τ for the potential shift (dashed blue) and the current shift (dashed red), respectively.

The potential drifts are all of the same order of magnitude, with a mean value of approximately 4.56 s. The data obtained from the first EC-STM measurement and the AGEF measurement fall within a comparable range, whereas the EC-SPM measurement (cf. Figure 5.20) deviates from the other data sets. This deviation may be attributed to differences in the experimental setup. Although the experimental conditions were nominally identical for all three measurements, the EC-SPM experiment was most exposed to the ambient atmosphere, as the sample holder was not mounted inside the microscope but positioned freely beneath it. In contrast, the EC-STM measurement may have experienced reduced exchange with the surrounding air due to the enclosed sample holder. The AGEF measurement exhibited the most stable experimental conditions.

The decay time constants associated with the current shift exhibit a considerably larger scatter; nevertheless, the AGEF measurement again

shows the most stable behavior. Overall, it can be concluded that the most stable measurement conditions were achieved using the AGEF potentiostat. The associated uncertainties for both the potential shift and the current shift are smallest for this setup.

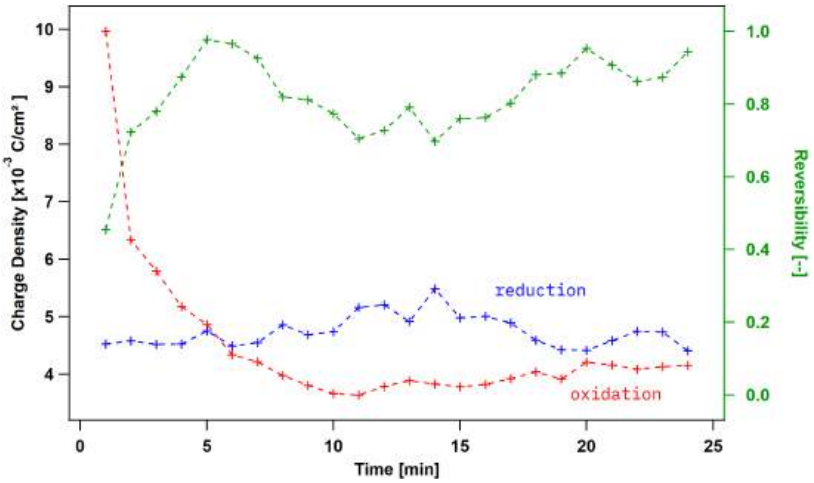

Figure 6.2: The figure presents the transferred charge density and the corresponding reversibility versus time as measured with the SPM 5500 potentiostat.

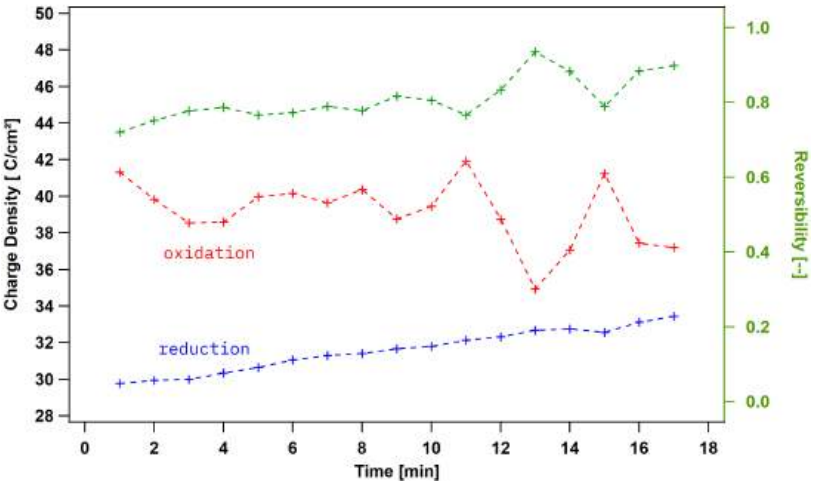

Figure 6.3: The figure presents the transferred charge density and the corresponding reversibility versus time as measured with the AGEF potentiostat.

When comparing the transferred charge densities normalized to the electrode area, it becomes apparent that they differ by approximately three orders of magnitude. The SPM 5500 potentiostat detects significantly lower transferred charges than the AGEF potentiostat. In addition, the temporal evolution of the oxidation process differs markedly between the two systems. In the SPM 5500 measurements, the transferred oxidation charge decreases and stabilizes after approximately 10 min, whereas the AGEF measurements exhibit a comparatively constant behavior that begins to fluctuate after about 10 min.

The reduction behavior is more stable than the oxidation behavior for both potentiostats. For the SPM 5500, the reduction-related charge density remains relatively constant at around 5 µC cm^{-2}. In contrast, the reduction charge density measured with the AGEF potentiostat increases continuously, reaching an overall change of approximately 2 C cm^{-2} within 16 min (0.125 C cm^{-2}s^{-1}).

The only parameter that appears to be directly comparable between the two systems is the reversibility. For both potentiostats, the reversibility

converges to values between approximately 80% and 100%.

At present, no direct correlation between the SPM data and the AGEF data can be established. Owing to the qualitative and quantitative differences observed in the cyclic voltammograms obtained from all three measurement setups, no definitive statement regarding the comparability of the instruments can be made. A uniform reference standard, for example in the form of a single-crystal electrode, would be required to enable meaningful conclusions about the respective systems.

6.2 STM-Data

As the STM was calibrated with HOPG prior to the measurements (see Section 4), it can be assumed that the imaging mode was operating correctly and that the acquired images possess sufficient interpretative significance. The STM data presented here clearly demonstrate that the SPM 5500 is capable of resolving different surface morphologies of (metallic) substrates. With appropriate experience and sufficient measurement time, imaging at near-atomic length scales can be achieved (see Figure 6.4).

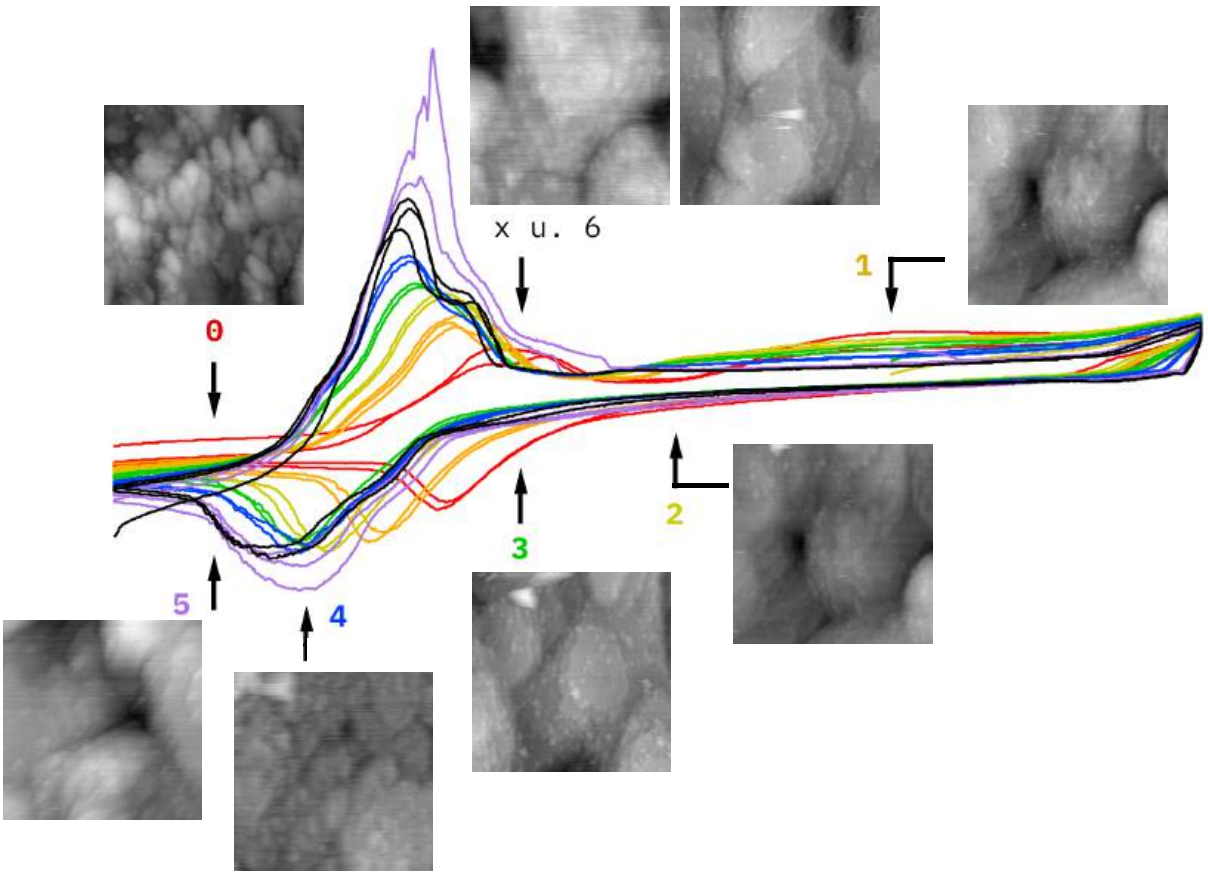

Figure 6.4: Combined representation of electrochemical and structural data. The cyclic voltammograms shown correspond to the dataset presented in Fig. 5.7 and are displayed using identical axis scaling. The numbered markers indicate the electrode potentials at which the STM measurements were performed. For each marked position, the corresponding STM image is shown, displaying the surface morphology of the gold thin film over an area of 100 nm × 100 nm at the respective electrochemical state. The STM images were selected from the corresponding trace/retrace pairs based on the lowest number of visible scanning artefacts in order to ensure optimal image quality. This image is a direct copy of Figure 5.17.

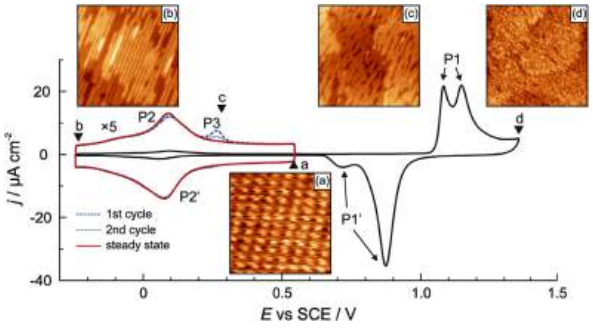

(a) Cyclic voltammograms (scan rate: 0.02 V s^{-1}) and potentiostatic STM images of Au(110) in 0.1 M H_2SO_4 reported by Yoshida *et al.*.[8] This figure served as the starting point for the measurements and as the conceptual basis for the present work.

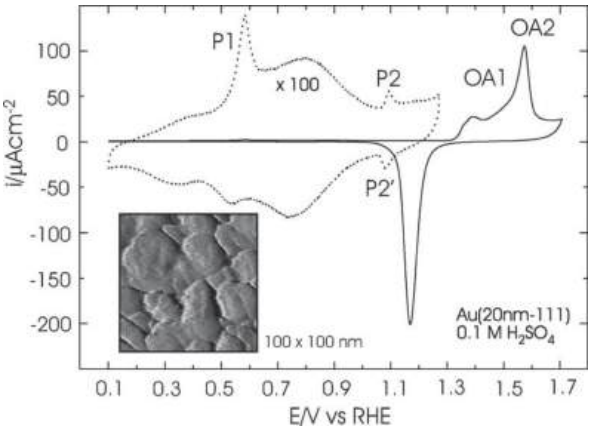

(b) Steady-state cyclic voltammograms of an Au(111) thin-film electrode (20 nm thickness) in contact with 0.1 M H_2SO_4, recorded at a scan rate of 10 mV s^{-1}. The double-layer region is indicated by the dotted line, while the oxidation/reduction region is shown as a solid line. The inset displays a representative ex situ STM image of the electrode immediately after electron-beam deposition of the 20 nm gold film, as reported by Wandlowski *et al.*[9].

As expected, the STM data obtained in this work do not directly coincide with the results reported by Yoshida *et al.* (cf. Figure 6.5a) or Wandlowski *et al.* (cf. Figure 6.5b). Although certain structural similarities may be suggested at first glance, complementary AFM measurements indicate that a fundamentally different surface system is investigated here. These differences are not limited to surface morphology - Yoshida investigated Au(110) and Wandlowski Au(111) surfaces - but also extend to the elemental composition of the samples. In particular, contributions from the titanium adhesion layer present in the thin-film system used in this work are likely to influence both the cyclic voltammograms and the observed surface structures.

Importantly, the primary objective of this work was not the direct reproduction of literature results, but the systematic evaluation of the EC-STM functionality of the SPM 5500 system under realistic laboratory conditions. The studies by Yoshida and Wandlowski therefore serve as methodological reference points rather than as quantitative benchmarks. Owing to limitations in experimental complexity, available instrumentation, and overall effort, the extensive sample preparation procedures and specialized setups described in the literature cannot be fully replicated within the scope of a master's thesis. The experiments presented here are thus intended as orienting and feasibility studies, aimed at assessing operational stability, data quality, and practical applicability of the EC-STM mode.

Accordingly, deviations from literature results are interpreted not as shortcomings, but as an inherent consequence of the different experimental focus and system configuration.

In addition to these methodological considerations, potential limitations related to the condition of the SPM 5500 hardware must be taken into account. Already in a previous study focusing on the implementation of the AFM mode, several components were found to exhibit significant wear. In particular, the AC-mode control unit was damaged and had to be removed from the setup in order to obtain a stable STM signal. Such

hardware-related constraints may further influence measurement quality and contribute to deviations from ideal experimental conditions, and should therefore be considered when interpreting the present results.

The images shown in Figure 6.4 provide clear evidence of a potential-driven reorganization of the surface morphology. In this respect, the experiment can be considered successful.

It should be noted that the STM and AFM data compare surface areas differing by a factor of 100 (Figure 6.6), which may explain why such pronounced structural inhomogeneity was not evident in the STM measurements (see fig. 6.6).

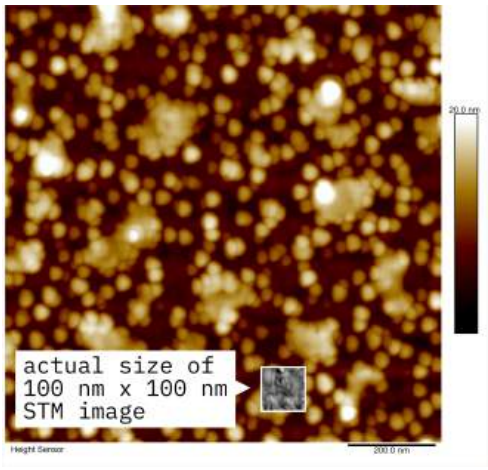

Figure 6.6: Comparison of image size STM (grayscale) vs AFM (brown scale).

Although atomic resolution could not be achieved on the gold thin-film sample, this limitation can be attributed to two main factors: On the one hand, the SPM 5500 system was operating close to its intrinsic resolution limits; on the other hand, the sample surface exhibited a high degree of inhomogeneity. For future measurements, the use of a single-crystal substrate is therefore recommended.

7 Conclusion and Future Work

In this work, the EC-STM mode of the SPM 5500 was systematically implemented and evaluated with respect to its functionality, stability, and practical applicability. As the first study within the research group to focus on EC-STM measurements, this thesis establishes a methodological foundation for future work with the instrument. The results demonstrate that the STM mode of the SPM 5500 is fully operational and capable of delivering meaningful surface images that clearly exhibit a dependence on the applied electrochemical potential. In this respect, the primary methodological objective of this thesis was successfully achieved.

Throughout the experiments, environmental parameters such as temperature and humidity were identified as critical factors influencing measurement stability. In particular, low humidity combined with elevated temperatures led to accelerated solvent evaporation in the electrochemical droplet cell, resulting in electrolyte concentration changes, loss of electrical contact, or irreversible damage to the working electrode. For future users, it is therefore strongly recommended to monitor environmental conditions closely. A practical and easily implementable countermeasure is the introduction of a moisture-saturated gas atmosphere, for example by passing nitrogen through a water-filled wash bottle into the environmental chamber, following the approach used in the AGEF measurements (see section 5.4). Preliminary test measurements suggest that this approach can significantly extend usable measurement times; however, a systematic validation of this method requires dedicated follow-up studies.

Although the electrochemical data obtained using the integrated SPM 5500 potentiostat did not quantitatively match those acquired with the external AGEF potentiostat, this discrepancy shows the limitations of the electrochemical part of the SPM 5500. The focus of this thesis was methodological rather than comparative. Nevertheless, future investigations would benefit from accessing raw electrochemical signals via the auxiliary data acquisition unit, allowing direct comparison between internally processed and externally recorded data. In this context, the use of simpler and well-defined reference systems is strongly advised.

The experiments further showed that both measurement duration and sample environment have a substantial impact on EC-STM data quality. For future studies, it is recommended that AFM and STM measurements be used in a complementary manner. AFM provides essential large-scale morphological information and enables reliable assessment of surface homogeneity, while STM allows detailed, potential-dependent investigations at higher spatial resolution. Combining both techniques is therefore crucial for obtaining a comprehensive understanding of the investigated surface systems.

As the internal data processing of the SPM 5500 is not fully known, the raw measurement data could, in principle, be accessed using the auxiliary data acquisition unit (Model: N9447A by Agilent Technologies). A direct comparison between externally acquired raw data and the internally

Figure 7.1: Photograph of the auxiliary data acquisition unit used to access internal signals of the SPM 5500. Via BNC connectors, the microscope can be directly connected to a digital storage oscilloscope (e.g., MephistoScope) for external signal readout.

processed data would therefore be feasible and could potentially lead to an improvement in the quality and reliability of the electrochemical data (see fig. 7.1).

Finally, the use of thin-film samples proved to be particularly challenging, with several samples being consumed during the course of this work. For researchers newly working with the SPM 5500, single-crystal substrates are recommended as a starting point, as they provide well-defined surface structures and facilitate a deeper understanding of the instrument's capabilities and limitations. Due to time constraints, this approach could not be pursued within the scope of the present thesis, but it represents a clear direction for future work.

Appendix

Unsuccessful Experiments and Coating Procedures

A

During this work and in preparation for it, a wide range of thin-film systems were investigated. In the following sections, these systems and the associated issues encountered during their use are documented in order to provide guidance for future users and to help avoid repetition of unsuccessful approaches.

All thin films discussed in this section were prepared in collaboration with the Optical Workshop of the University of Duisburg-Essen under the supervision of Martin Jermann[1].

1: It should be noted that the optical workshop performs excellent work in the fabrication of high-quality mirrors; however, the requirements for electrochemical experiments differ substantially from those for optical applications. I'm thankfull for Mr. Jermanns time and expertise.

The fabrication of thin films is inherently challenging, and their handling—particularly in electrochemical environments—requires careful optimization and experience.

Au on Si wafers

Gold films can be deposited directly onto silicon wafers; however, sufficient adhesion is not achieved without an intermediate adhesion layer. Even minor mechanical stress, such as the placement of an O-ring during the assembly of a liquid cell, leads to delamination of the gold film from the silicon substrate. Even working in mild conditions like 0.05 M H_2SO_4 damages the surface visibly (see fig. A.1).

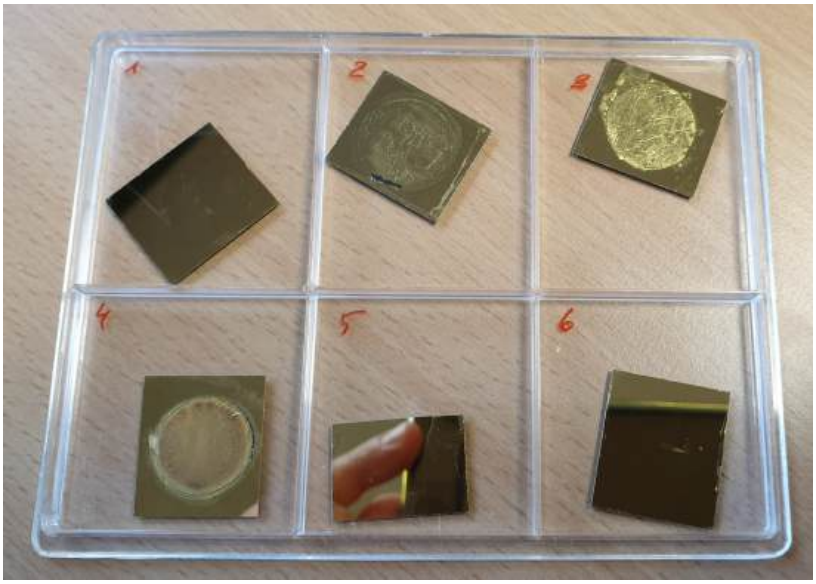

Figure A.1: Six Au-on-Si samples stored in a sample box are shown. For samples 2, 3, and 4, pronounced visual changes of the gold film are evident after the experiments. Samples 2 and 4 additionally exhibit damage caused by an O-ring in contact with the surface during the measurements using a different setup. Samples 5 and 6 have not yet been used.

Au on glass

Several gold-on-glass samples were examined during this work. These films exhibited a surface roughness that was too high for stable STM measurements, frequently causing saturation of the STM feedback loop. In addition, the films were not fully closed, rendering them unsuitable for EC-STM experiments. The electrolyte was able to readily penetrate

between the film and the glass substrate, thereby causing damage to the film (see A.2).

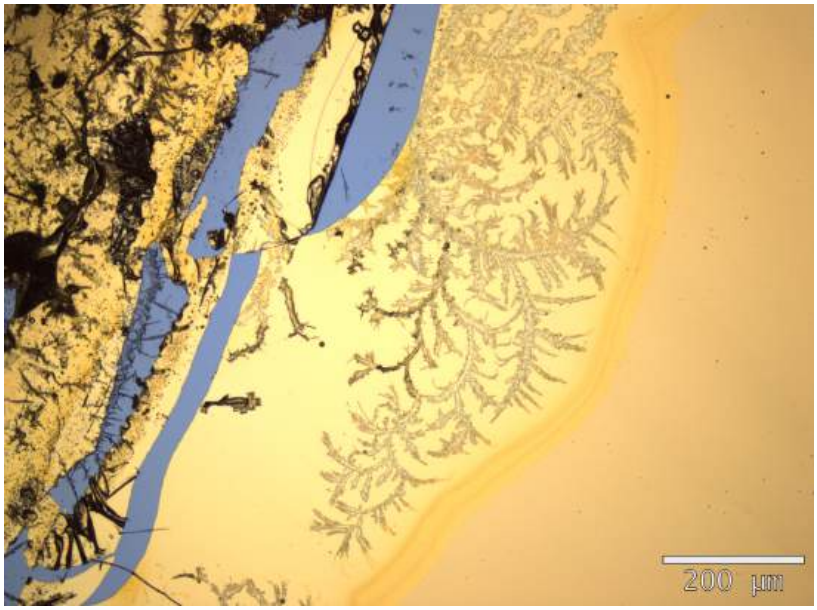

Figure A.2: Shown is a reflected-light optical microscope image (10× magnification, Olympus BX41) of a gold-on-glass film. In addition to flake-like delamination at the left edge, feather-like structures are visible that resemble filiform corrosion, which is also observed macroscopically in delaminating paint coatings. The formed channels act as capillaries and promote electrolyte penetration, thereby facilitating further delamination of the film from the substrate.

Ni on glass

Nickel-on-glass films were among the most extensively studied systems, alongside the Si-Ti-Au films used in this work, and were already employed during the physical chemistry master laboratory course. These films showed highly variable stability. While some samples allowed the construction of electrochemical cells that remained stable for several tens of minutes, others from the same batch delaminated almost immediately upon contact with an electrolyte.

This behavior was observed independently of the electrolyte pH. Tests conducted with 1 M KOH, 0.1 M H_2SO_4, and Milli-Q water all resulted in delamination of the nickel film from the glass substrate within minutes, or even instantaneously.

Further investigation revealed that the deposition process and substrate preparation are critical factors determining film quality. Despite extensive physical and chemical cleaning procedures, including piranha treatment, the glass substrates exhibited regions of reduced surface energy. As a result, the deposited films were not uniformly closed. These defects allow the electrolyte to diffuse between the film and the substrate, ultimately leading to delamination and destruction of the sample.

Similar effects were previously observed on a macroscopic scale during undergraduate studies, where insufficient substrate preparation led to defective coatings in paint systems. In all cases, inadequate surface preparation was identified as the primary cause.

Ongoing efforts by Martin Jermann to improve film quality through alternative cleaning methods and deposition processes have already yielded some improvements. However, optical transmission microscopy at 5× magnification revealed that the films still contained defects and

therefore remain unsuitable for electrochemically based experiments (e.g. fig. A.3).

Overall, the results presented in this appendix highlight the critical importance of sample quality for EC-STM experiments. Only the Si-Ti-Au thin films employed in the present work provided sufficient stability and homogeneity to enable meaningful measurements.

Figure A.3: Shown is a transmitted-light optical micrograph (5× magnification, Olympus BX41) of a nickel film on a glass substrate. Even at the lowest magnification, transmitted light reveals that the film is not continuous and penetrated by holes of different sizes.

Bibliography

[1] *BASE - Fukushima*. [Online; accessed 2025-08-01]. URL: https://www.base.bund.de/de/nukleare-sicherheit/nukleare-unfaelle/fukushima/fukushima-unfall_inhalt.html (cited on page 1).

[2] *Archiv der Bundesregierung | Die Energiewende*. [Online; accessed 2025-08-01]. URL: https://www.bundesregierung.de/statisch/jb11-12/Webs/Breg/DE/Themen/Jahresbericht_2011_2012/03_Energie/1_Energiewende/_node.html (cited on page 1).

[3] Bundesministerium für Wirtschaft und Klimaschutz. *One-Stop-Shop - Wasserstoff - Die Nationale Wasserstoffstrategie*. [Online; accessed 2025-08-11]. URL: https://www.bundeswirtschaftsministerium.de/Redaktion/DE/Wasserstoff/Dossiers/wasserstoffstrategie.html (cited on page 1).

[4] *MPI für Polymerforschung*. [Online; accessed 2025-07-12]. URL: https://www.mpip-mainz.mpg.de/ (cited on page 1).

[5] *Welcome to the Domke Group*. [Online; accessed 2025-07-12]. URL: https://www.uni-due.de/chemie/akdomke/ (cited on page 1).

[6] *Kons & Pusnik: Umzug und Möbeltransport Duisburg*. [Online; accessed 2025-07-12]. URL: https://www.kons-pusnik.de/ (cited on page 1).

[7] *Keysight 5500 Scanning Probe Microscope*. Rev F, August 2014. Santa Rosa, CA 95403: Keysight Technologies, 2012 (cited on pages 1, 2, 4, 5, 10, 13, 14, 20).

[8] Koji Yoshida et al. "Reconstruction and Electrochemical Oxidation of Au(110) Surface in 0.1 M H2SO4". In: *Electrochimica Acta* 139 (2014), pp. 281–288. DOI: 10.1016/j.electacta.2014.06.162 (cited on pages 2, 5, 14, 25, 26, 29, 36, 54).

[9] Th Wandlowski et al. "Surface Enhanced Infrared Spectroscopy—Au(1 1 1-20nm)/Sulphuric Acid—New Aspects and Challenges". In: *Electrochimica Acta* 49.8 (Mar. 2004), pp. 1233–1247. DOI: 10.1016/j.electacta.2003.06.002. (Visited on 01/21/2025) (cited on pages 2, 5, 14, 25, 26, 36, 54).

[10] Wikipedia. *Hubert Laitko — Wikipedia, die freie Enzyklopädie*. [Online; Stand 15. September 2024]. 2025. URL: https://de.wikipedia.org/w/index.php?title=Hubert_Laitko&oldid=254526390 (cited on page 3).

[11] Werner Schröter, Karl-Heinz Lautenschläger, and Hildegard Bibrack. *CHEMIE - Fakten Und Gesetze*. 11. Auflage. Leipzig: VEB Fachbuchverlag, 1979 (cited on page 3).

[12] Peter W. Atkins, ed. *Physikalische Chemie. Hauptbd.* 4., vollst. überarb. Aufl., 2. Nachdr. Weinheim: Wiley-VCH, 2012 (cited on page 3).

[13] Wikipedia contributors. *Scanning tunneling microscope — Wikipedia, The Free Encyclopedia*. [Online; accessed 12-09-2025]. 2025. URL: https://en.wikipedia.org/w/index.php?title=Scanning_tunneling_microscope&oldid=1326766297 (cited on pages 4, 5).

[14] Allen J. Bard and Larry R. Faulkner. *Electrochemical Methods: Fundamentals and Applications*. 2. edition. New York Weinheim: Wiley, 2001 (cited on page 4).

[15] Noémie Elgrishi et al. "A Practical Beginner's Guide to Cyclic Voltammetry". In: *Journal of Chemical Education* 95.2 (Feb. 2018), pp. 197–206. DOI: 10.1021/acs.jchemed.7b00361 (cited on page 6).

[16] Wikipedia. *Potentiostat — Wikipedia, die freie Enzyklopädie*. [Online; accessed 12-09-2025]. 2025. URL: https://de.wikipedia.org/w/index.php?title=Potentiostat&oldid=252990871 (cited on page 6).

[17] Wikipedia contributors. *Cyclic voltammetry — Wikipedia, The Free Encyclopedia*. https://en.wikipedia.org/w/index.php?title=Cyclic_voltammetry&oldid=1320010436. [Online; accessed 12-09-2025]. 2025 (cited on page 7).

[18] Meilhaus Electronic GmbH. *MEphisto Scope UM202/UM203 - Meilhaus Electronic*. [Online; accessed 2025-08-12]. URL: https://www.meilhaus.de/mephisto-scope-um202-um203.htm (cited on page 11).

[19] Keysight. *PicoView Software | Keysight*. [Online; accessed 2025-02-17]. URL: https://www.keysight.com/de/de/lib/software-detail/instrument-firmware-software/picoview-software.html (cited on page 14).

[20] Jean «d'» Ans and Ellen Lax. *Taschenbuch für Chemiker und Physiker. 1. Makroskopische physikalisch-chemische Eigenschaften*. ger. 3., völlig neu bearb. Aufl. Berlin [u.a: Springer, 1967 (cited on page 15).

[21] Peter Münster. "Abbildungsprozesse beim STM auf atomarer Skala Simulation und Experimente". Diplomarbeit. Kalsruhe: Kalsruhe, Sept. 29, 1997 (cited on pages 17, 18).

[22] B Winzer. *Untersuchung und Modifizierung organischer Molekülschichten mit dem Raster-Tunnel-und Raster-Kraftmikroskop in*. 1992 (cited on page 17).

[23] Sang-Il Park and C. F. Quate. "Tunneling Microscopy of Graphite in Air". In: *Applied Physics Letters* 48.2 (Jan. 13, 1986), pp. 112–114. DOI: 10.1063/1.96968. (Visited on 09/28/2025) (cited on page 17).

[24] StudioX. *HOPG-ZYA by MikroMasch*. URL: https://www.spmtips.com/test-structures-HOPG-ZYA (visited on 09/28/2025) (cited on page 17).

[25] David Tománek et al. "Theory and Observation of Highly Asymmetric Atomic Structure in Scanning-Tunneling-Microscopy Images of Graphite". In: *Physical Review B* 35.14 (May 15, 1987), pp. 7790–7793. DOI: 10.1103/PhysRevB.35.7790. (Visited on 09/28/2025) (cited on page 17).

[26] Rubén del Barrio-Galán et al. "Dissolved Oxygen Removal in Wines by Gas Sparging, Its Optimization and Chemical Impact". In: *Beverages* 10.1 (2024). DOI: 10.3390/beverages10010003 (cited on page 26).

[27] *Smoothing*. [Online; accessed 2025-09-11]. URL: https://www.wavemetrics.com/products/igorpro/dataanalysis/signalprocessing/smoothing (cited on page 43).

[28] *Untitled*. [Online; accessed 2025-11-19]. URL: https://www.uni-due.de/imperia/md/content/ican/ican-broschuere_2020.pdf (cited on page 47).

UNIVERSITÄT DUISBURG ESSEN

Offen im Denken

Eidesstattliche Versicherung

Hiermit versichere ich an Eides Statt, dass ich diese Arbeit bzw. im Fall einer Gruppenarbeit den von mir entsprechend gekennzeichneten Anteil an der Arbeit selbständig verfasst habe. Ich habe keine unzulässige Hilfe Dritter in Anspruch genommen. Zudem habe ich keine anderen als die angegebenen Quellen und Hilfsmittel benutzt und alle Ausführungen (insbesondere Zitate), die anderen Quellen wörtlich oder sinngemäß entnommen wurden, kenntlich gemacht.

Ich versichere, dass die von mir in elektronischer Form eingereichte Version dieser Arbeit mit den eingereichten gedruckten Exemplaren übereinstimmt.

Mir ist bekannt, dass im Falle eines Täuschungsversuches die betreffende Leistung als mit "nicht ausreichend" (5,0) bewertet gilt. Zudem kann ein Täuschungsversuch als Ordnungswidrigkeit mit einer Geldbuße von bis zu 50.000 Euro geahndet werden. Im Falle eines mehrfachen oder sonstigen schwerwiegenden Täuschungsversuchs kann ich zudem exmatrikuliert werden.

Mir ist bekannt, dass sich die Prüferin oder der Prüfer bzw. der Prüfungsausschuss zur Feststellung der Täuschung des Einsatzes einer entsprechenden Software oder sonstiger elektronischer Hilfsmittel bedienen kann.

Ich versichere an Eides Statt, dass ich die vorbenannten Angaben nach bestem Wissen und Gewissen gemacht habe und dass die Angaben der Wahrheit entsprechen und ich nichts verschwiegen habe.

Die Strafbarkeit einer falschen eidesstattlichen Versicherung ist mir bekannt, insbesondere die Strafandrohung gemäß §§ 156, 161 StGB, auf welche ich konkret hingewiesen wurde.

§ 156 Falsche Versicherung an Eides Statt

Wer vor einer zur Abnahme einer Versicherung an Eides Statt zuständigen Behörde eine solche Versicherung falsch abgibt oder unter Berufung auf eine solche Versicherung falsch aussagt, wird mit Freiheitsstrafe bis zu drei Jahren oder mit Geldstrafe bestraft.

§ 161 Fahrlässiger Falscheid; fahrlässige falsche Versicherung an Eides Statt

(1) Wenn eine der in den §§ 154 bis 156 bezeichneten Handlungen aus Fahrlässigkeit begangen worden ist, so tritt Freiheitsstrafe bis zu einem Jahr oder Geldstrafe ein.
(2) Straflosigkeit tritt ein, wenn der Täter die falsche Angabe rechtzeitig berichtigt. Die Vorschriften des § 158 Abs. 2 und 3 gelten entsprechend.

_____

Ort, Datum Unterschrift